




Open Archive Toulouse Archive Ouverte (OATAO)

OATAO is an open access repository that collects the work of Toulouse researchers and makes it freely available over the web where possible.

This is an author-deposited version published in: <http://oatao.univ-toulouse.fr/>
Eprints ID: 18310

To cite this version: Granados-Ortiz, Francisco-Javier and Lai, Choi-Hong and Pérez Arroyo, Carlos and Puigt, Guillaume and Airiau, Christophe  *Uncertainty Quantification and Sensitivity Analysis applied to an under-expanded single jet*. (2016) In: 46th AIAA Fluid Dynamics Conference, 13 June 2016 - 17 June 2016 (Washington, United States)

Any correspondence concerning this service should be sent to the repository administrator:
staff-oatao@listes-diff.inp-toulouse.fr

Uncertainty Quantification and Sensitivity Analysis Applied to an Under-expanded Single Jet

F.-J. Granados-Ortiz* and C.-H. Lai †

University of Greenwich, Old Royal Naval College, Park Row, SE10 9LS, London (U.K.)

C. Pérez Arroyo ‡ and G. Puigt §

CERFACS, Computational Fluid Dynamics Team, 42 avenue Coriolis, 31057 Toulouse Cedex (France).

C. Airiau ¶

*IMFT, Université de Toulouse, UMR 5502 CNRS/INPT-UPS, Allée du professeur Camille Soula,
31400 Toulouse (France)*

The aim of CFD simulations is to model and compute the ideal performance of a flow under some particular conditions. A classic approach is to perform simulations with fixed parameters and boundary conditions. However, this is not accurate enough due to the fact that under realistic conditions, some parameters may be uncertain. In recent years, the interest of undertaking the simulations under uncertainty is increasing, but is not yet a common rule and 'incomplete' simulations are still taking place. This procedure could be missing information such as whether mechanical tolerances are influential in dramatic parts of the flow or the relevancy in accurate tuning of turbulence models. Taking this knowledge into consideration, Non-Intrusive Uncertainty Quantification (UQ) has been applied to 3D RANS simulations of an under-expanded jet, in order to understand the impact of input uncertainties. Results show that some regions of the jet plume are very sensitive to a combination of both physical and turbulence model variance. These regions are in fact corresponding to the parts of the jet where screech and shock-cell noise is generated, so this can be an indicator of a relevant impact of uncertainties in jet noise emission, what can guide to future research and more robust developments in aircraft industry.

I. Introduction and motivation

It is a regular practice in Computational Fluid Dynamics (CFD) to analyse the scenario performance of fluids by undertaking simulations with fixed parameters in the set-up configuration. However, this can be often an incomplete approach. When a classic code is used to mimic the physics of a flow, it does not take into account the associated uncertainties such as geometrical adaptation, grid uncertainty, domain size, numerical convergence, manufacturing tolerances or uncertainty of the measurement devices. Not taking into account those inaccuracies can result to misleading or incomplete engineering conclusions. This gives rise to the need of providing error measurements in CFD, as most experimentalists do.

In this work, Non-Intrusive Uncertainty Quantification (UQ) techniques are implemented to demonstrate the inclusion of inaccuracies in input parameters affect the output from Reynolds-averaged Navier-Stokes (RANS) simulations and how this can be used to gain more information about the performance in conjunction with Sensitivity Analysis (SA), that is about apportioning the output variance. To the knowledge of the

*Marie Curie Research Fellow in the Numerical and Applied Mathematics Research Unit at University of Greenwich.

†Professor of Numerical Mathematics at University of Greenwich.

‡Marie Curie Research Fellow in CERFACS CFD team.

§Senior Researcher in CERFACS CFD team.

¶Professor at University of Toulouse/IMFT

authors, there is no literature about UQ on jets in the presence of shock-cells, despite that it has already been developed to an underexpanded jet in a crossflow for turbulent mixing,¹ to quantify physical uncertainties in transonic airfoils to point out the importance of the sensitivity of shocks² or to uncertainties in the turbulence models for transonic wall-bounded flows.³

In compressible supersonic jets this is a particularly interesting analysis, as small changes in input parameters may lead to sensitive variations in relevant flow features and the noise emission,⁴ which currently represents a major concern in robust design because of environmental regulations and the challenge of perceived noise reduction of 65% by 2050 with respect to the values dated from the year 2000.⁵

Non-Intrusive UQ methods have been applied to 3D RANS simulations with *elsA* solver,⁶ whose set-up is described in Section II. Due to the fact that common sampling methods such as Monte-Carlo are impractical in terms of computational cost, UQ will be deployed with two different approaches. First, generalised Polynomial Chaos (gPC)⁷ is to be applied in order to study the uncertainty in Section III.B. Second, in order to have another method for comparison, Kriging surrogates are built in Section III.C to ensure the quality of the analysis. In Section IV, a sensitivity analysis is conducted with both methods, in order to assign to each input uncertainty its contribution to the total variance.

The results presented in this work demonstrate the jet plume can very sensitive to a combination of both the physical and turbulent model uncertainties prescribed. The influence in the nozzle lip vicinity and in the shock-cell areas is particularly interesting since this can be influencing screech and shock-cell noise respectively. These conclusions can be an important outcome which can help understand how the noise emission and flow features are being affected by input uncertainties and lead to future research in aircraft industry robust design.

II. CFD simulations

A. Numerical formulation

The full three-dimensional compressible Reynolds-Averaged Navier-Stokes equations in conservative form are solved by using the Finite Volume multi-block structured solver *elsA* (Onera’s software⁶). The turbulence model used in the computations is the one-equation Spalart-Allmaras standard model.⁸ The convective flux is computed using an upwind approach based on the Roe’s approximate Riemann solver.⁹ The scheme’s accuracy is increased by the use of either a second order MUSCL extrapolation¹⁰ coupled with the minmod limiter or a third order extrapolation technique.¹¹ The last technique does not include any limiter but, as it will be shown in the next sections, the convergence of the steady solutions does not suffer from this numerical parameter. Finally, Harten correction¹² is included to avoid non-entropic solutions. The convection term of the Spalart-Allmaras turbulence model is discretized following the formalism of Larotourou,¹³ by using the sum of a centered approximation and a stabilizing (dissipation) term. The diffusion scheme is based on a centred formulation used in conjunction with a correction that is introduced to remove the odd/even decoupling and damp high frequency waves. For attaining efficiently steady state solutions, the backward Euler time integration is coupled with a V-type multigrid technique with three levels of coarsening. The implicit system is solved at $CFL = 100$ with a $LU - SSOR$ algorithm with four sweeps.¹⁴ A minimum of 4-6 drops of order of magnitude in the residuals is obtained for all the simulations after 10000 multigrid cycles. In order to accelerate the convergence for all the conditions, a converged deterministic base case solution has been used as initial solution.

B. Simulation set-up

The case of study is one of a cold supersonic under-expanded single jet that was tested experimentally by André.¹⁵ The jet is produced from a convergent nozzle with an exit diameter of $D = 38.0mm$ and a modelled nozzle lip thickness of $t = 0.125D$. The nozzle is operated under-expanded at the stagnation to ambient pressure ratio $NPR = p_s/p_{amb} = 2.27$. The Reynolds number, Re , based on the jet exit diameter is 1.25×10^6 and the fully expanded jet Mach number is $M_j = 1.15$. The perfectly expanded Mach number, *i.e.* the Mach number that would be reached if the jet was able to expand further to ambient conditions, is related to the

total pressure by

$$NPR = \frac{p_s}{p_{amb}} = \left(1 + \frac{\gamma - 1}{2} M_j^2\right)^{\gamma/(\gamma-1)}. \quad (1)$$

The boundary conditions used in the computations are as follows. The interior/exterior and lip walls of the nozzle are computed with adiabatic no-slip wall conditions. A characteristic approach is chosen to define the inflow conditions outside the nozzle. Such a condition works for all configurations (inflow/outflow, subsonic/supersonic): the number of fields to impose (1, 4 or 5) is chosen according to the local analysis of the waves that travel across the interface. The remaining lateral and outlet boundary conditions are set to a subsonic characteristic one, where the reference ambient pressure is defined.

The computational domain used for the RANS simulations extends $100D$ in the axial direction and $50D$ in the radial direction. The interior of the nozzle is modeled up to $6D$ while the exterior up to $9D$.

C. Mesh generation

The converged mesh consists in a butterfly type mesh to avoid the singularity at the axis as shown in Fig. 1 (b). It contains 20×10^6 cells with roughly $(900 \times 300 \times 64)$ cells in the axial, radial and azimuthal directions respectively forward to the nozzle exit plane, $(220 \times 120 \times 64)$ inside the nozzle and $(170 \times 100 \times 64)$ outside.

The nozzle is wall-resolved for all the conditions with $y^+ \approx 1$ and radially stretched up to the end of the domain at a rate of 10% as can be seen in Fig. 1 (a). Axially, the mesh is uniform at the exit of the nozzle, then it is stretched at 6% up to $0.25D$. Next, it is kept constant up to $10D$, in order to have a minimum of around 40 cells per shock-cell (measured at the last cell, which due to the flow physics, it is the most shortened shock-cell). The mesh is axially stretched again up to the end of the domain at a rate of 10%.

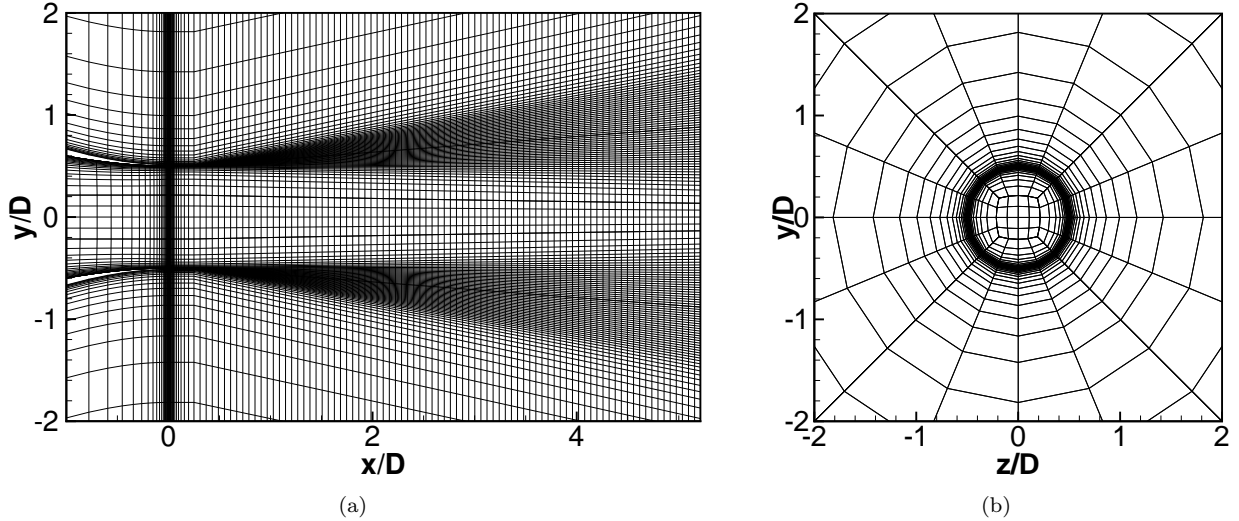


Figure 1. Mesh cuts representing every fourth cells in the plane (a) $z/D = 0$ and the plane (b) $x/D = 0$

Having a converged mesh for all deterministic simulations required for uncertainty quantification is a must. This need is specially important for flows containing shocks. In this under-expanded jet, the shock-cells are actually a series of expansion and compression waves that look like widen shocks. The above mentioned mesh has been thoroughly obtained with the following convergence procedure using as reference parameter the Mach number profile at the axis for the deterministic base case and conditions with a higher NPR . First, the mesh has been converged azimuthally with 64 cells, obtaining a relative error with respect to a refined mesh of less than 0.15% as shown in Fig. 2 (a). Second, the axial discretization is taken into account by varying the starting position, where the mesh topology is uniform. Axial convergence is obtained with an error of 0.2% with respect to the most refined mesh for the position of $0.25D$ as shown in Fig. 2 (b). Finally, the y^+ has been checked so that it still lays in the range smaller than unity for the range of working conditions.

The simulations are carried out with the third order extrapolation as mentioned in Section II.A. The fact that the shock-cells are not discontinuous but weak shocks and that they are discretized over 40 cells allows

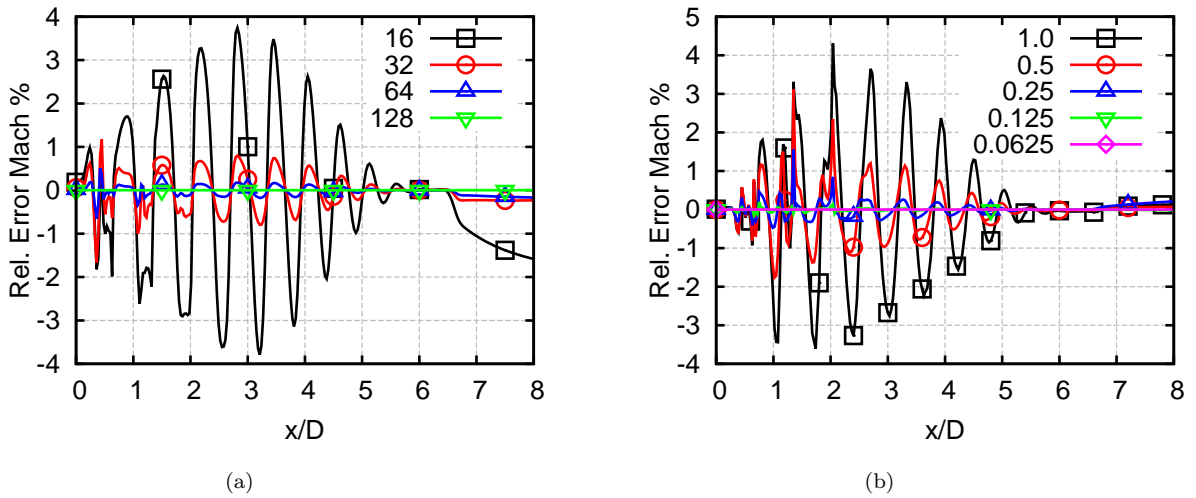


Figure 2. Mach number profile relative error of the deterministic base case at the axis for (a) different azimuthal discretizations, where each line represents the number of azimuthal nodes, and (b) different axial discretizations, where each line represents the starting position where the mesh is uniform. The refined mesh has been used as converged solution.

for the use of such high order scheme without any shock limiter. The Mach profile at the axis using the second order extrapolation is compared with the third order one in Fig. 3. The second order extrapolation is, as expected, more dissipative, which reinforces the use of the third order extrapolation. Also a contour plot of the definitive CFD simulation can be seen in Figs. 4 and 5, where only a region of the extensive computational domain is shown.

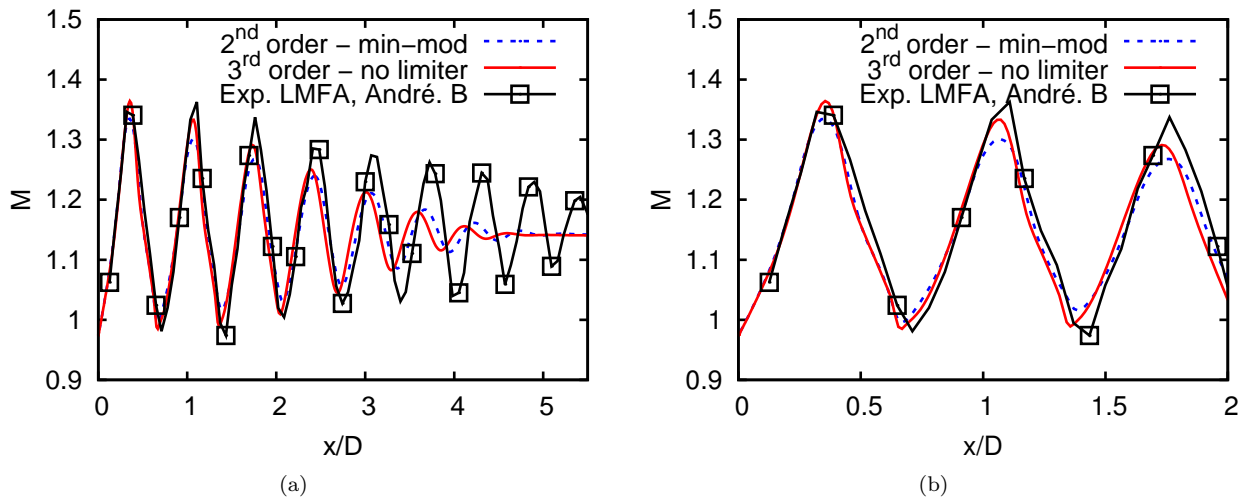


Figure 3. Mach number profile of the deterministic base case at the axis for (a) a general view and (b) a detailed view of the first three shock-cells.

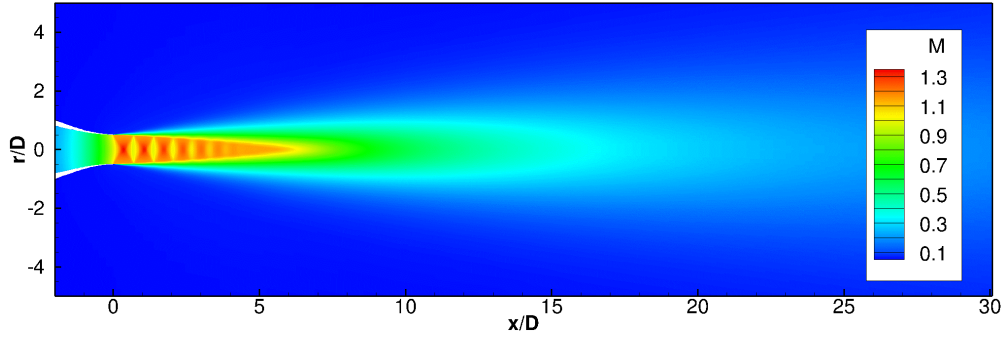


Figure 4. CFD RANS simulation of the Mach number from the deterministic base case of the under-expanded jet in *elsA*.

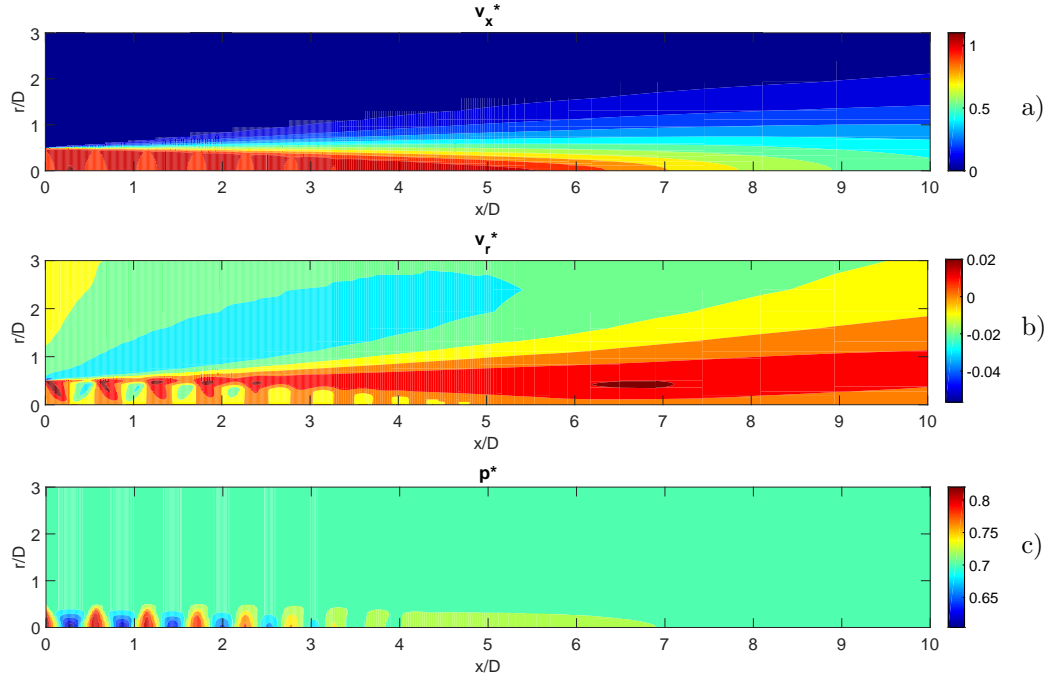


Figure 5. CFD RANS simulations of the deterministic base case of the under-expanded jet in *elsA*. The shown parameters are (a) the dimensionless axial velocity profile, $v_x^* = v_x/c_{ref}$, (b) dimensionless radial velocity profile, $v_r^* = v_r/c_{ref}$ and (c) dimensionless static pressure, $p^* = \frac{p}{\gamma_{ref} p_{ref}}$, with $\gamma = 1.4$ the specific heat ratio, $p_{ref} = 98000 Pa$ the reference pressure and $c_{ref} = 340.26 m/s$ the reference speed of sound.

III. Uncertainty Quantification

The main purpose of this work is to compute both the impact of uncertainty from a jet facility and the computational injection of turbulence, that give a stochastic point of view to the problem, rather than the classical deterministic one. This leads to the concepts of Uncertainty Quantification and Sensitivity Analysis, which involves the study of how uncertainty in the output of a model (numerical or otherwise) can be apportioned to different sources of uncertainty in the model input¹⁶ (see Figure 6). In this section, the input uncertainties are described as well as the mathematical methods used for their handling.

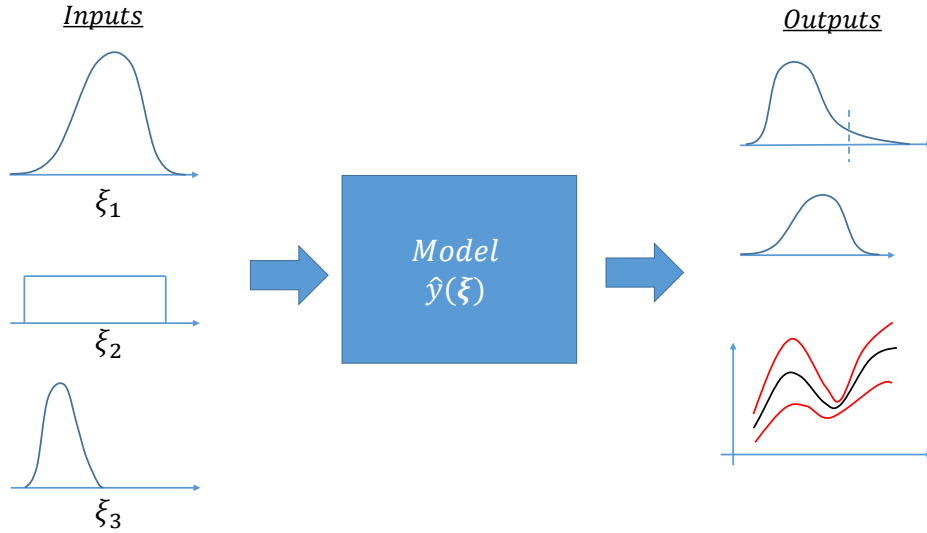


Figure 6. Propagation of uncertainty throughout a mathematical model.

A. Tests and Prescription of Uncertainties

The parameters treated as stochastic inputs for uncertainty quantification are the stagnation pressure, p_s , and the turbulent to laminar viscosity ratio, $R_t = \mu_t/\mu$, that are both imposed at the inlet of the nozzle. These parameters have been selected because of their stochastic behavior in nature.

The stagnation pressure is used to model the uncertainty in the mass-flow rate. Such decision is based on suggestions from the experimentalists at von Karman Institute for Fluid Dynamics. For them, during a single run, notable pressure variations are not yet expected due to emptying of the tanks. However, these are expected during repeated tests. This is because of the membranes of the valves are opening and closing several times, and the displacements of these membranes can be slightly different for each run, leading to variations in the mass-flow rate. Moreover, we have to take into account the uncertainty of the measurement devices (pressure sensors). Consequently, a conservative range of $\pm 5\%$ has been agreed with experimentalists. To sum up, the chosen probabilistic distribution is $p_s \sim U(0.95\bar{p}_s, 1.05\bar{p}_s) = U(211337, 233583) Pa$, where \bar{p}_s refers to the deterministic base value $\bar{p}_s = 222460 Pa$.

The second parameter is the laminar to turbulent viscosity ratio, $R_t = \mu_t/\mu$, used for the injection of turbulence in the Spalart-Allmaras model,⁸ which is in fact a computational input for the turbulence at the exit of the nozzle. This parameter stays fixed when simulating the operating conditions of an experimental facility. However, treating it as a deterministic parameter is not appropriate, as the flow properties can be sensitive. Thus to quantify the change in the simulations is relevant. Therefore, the variation of the parameter has been carefully chosen based on several tests on the CFD solver, for which the solution is close to experimental results. By increasing this parameter at the inlet, it increases also the maximum non dimensional turbulent wall unit, y^+ , achieved at the wall near the exit. Nevertheless, the y^+ remains of order unity changing from 1 to 6 for the higher R_t value. Figs. 7 and 8 show the Mach and R_t profiles for different R_t inlet values, respectively. Fig. 9 shows the impact on the axial velocity profile at $x = 2mm$, and it is compared with the available experimental data. The values are non-dimensionalized by the maximum values due to the fact that the experimental data corresponds to a subsonic test case ($M_e = 0.9$). Moreover, the experimental values lacked of the position of the probes and therefore, a curve translation has been done to match the computational results. The chosen probabilistic distribution is $R_t \sim U(2.2, 220)$. This is because for smaller values of R_t the change in the injection of turbulence is too small and there is no need to include it in the study. The deterministic base value is $R_t = 2.2$, as this was the value used by the authors in the initialisation of the flow for a Large Eddy Simulation (LES).^{17,18}

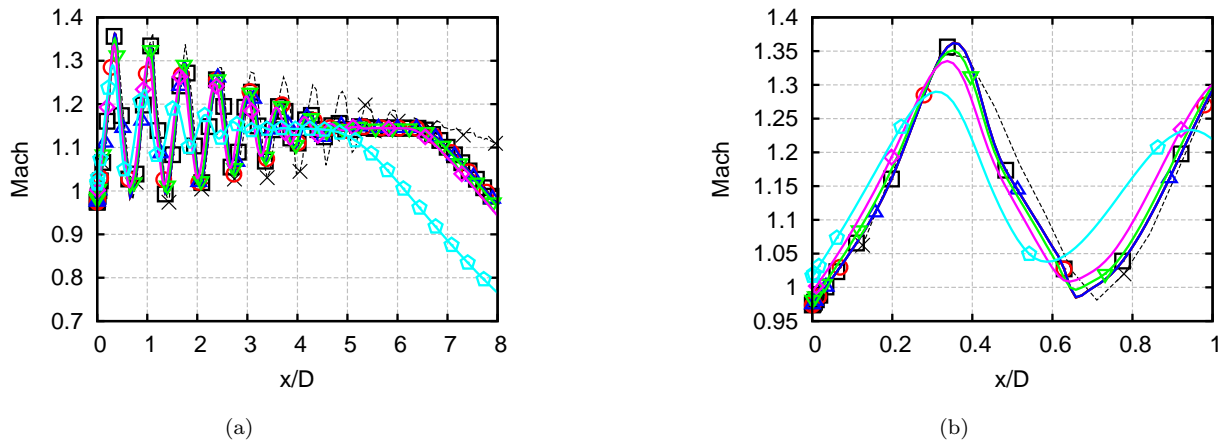


Figure 7. Mach number profile of the deterministic base case at the axis for different R_t inlet values in a (a) general and a (b) detailed view. $R_t = 0.022$ \square , $R_t = 0.22$ \circ , $R_t = 2.2$ \triangle , $R_t = 22$ ∇ , $R_t = 220$ \diamond , $R_t = 2200$ \circ .

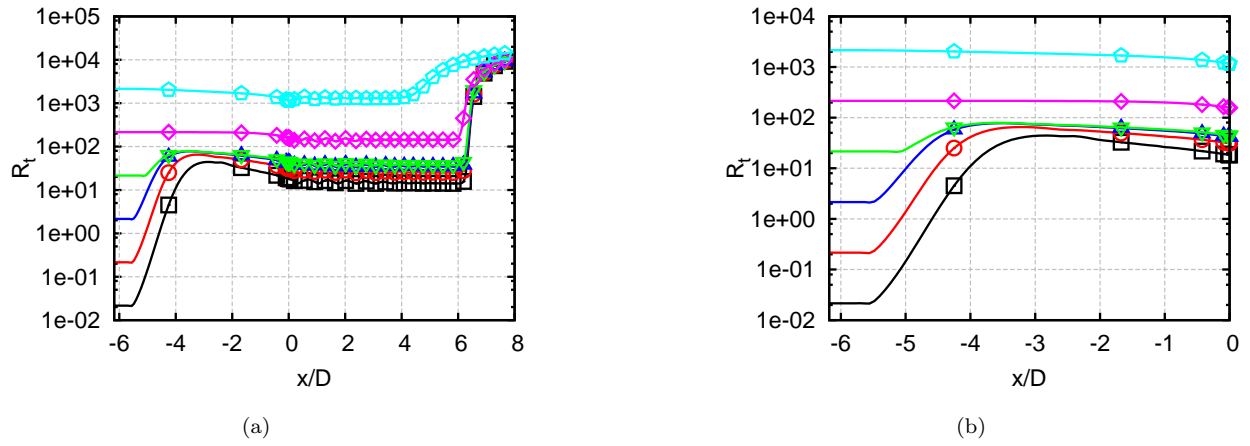


Figure 8. R_t profile of the deterministic base case at the axis for different R_t inlet values in a (a) general and a (b) detailed view. $R_t = 0.022$ \square , $R_t = 0.22$ \circ , $R_t = 2.2$ \triangle , $R_t = 22$ ∇ , $R_t = 220$ \diamond , $R_t = 2200$ \circ .

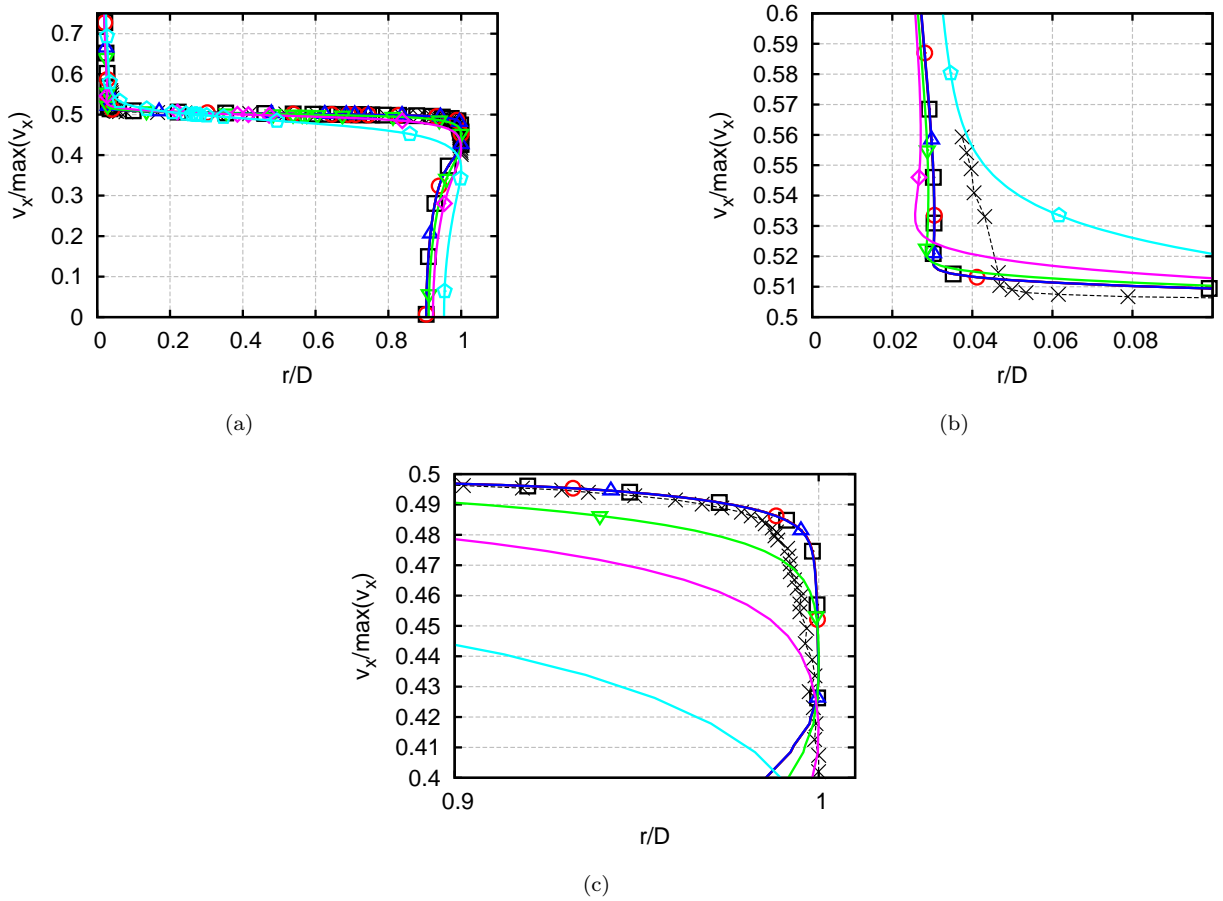


Figure 9. Axial velocity profile of the deterministic base case at the axis for different Re inlet values in a (a) general and a (b)&(c) detailed view. *Experimental* \times , $Re = 0.022$ \square , $Re = 0.22$ \circ , $Re = 2.2$ \triangle , $Re = 22$ ∇ , $Re = 220$ \diamond , $Re = 2200$ \circ .

B. Generalised Polynomial Chaos for Uncertainty Quantification

Uncertainty quantification (UQ) has become a very influential field, due to the fact that methods developed in these years bring the possibility of understanding how the behaviour of expensive (normally in terms of computation) mathematical models is being affected by imprecisely defined inputs. For a more formal explanation, let consider the differential operator on an output of interest of a stationary problem, $y(\mathbf{x}, \boldsymbol{\xi}(\eta))$ as

$$\mathcal{L}(\mathbf{x}, \boldsymbol{\xi}(\eta); y(\mathbf{x}, \boldsymbol{\xi}(\eta))) = \mathcal{Q}(\mathbf{x}, \boldsymbol{\xi}(\eta)), \quad (2)$$

with \mathcal{L} and \mathcal{Q} differential operators on $\mathcal{D} \times \Xi$, where $\mathbf{x} \in \mathcal{D} \subset \mathbb{R}^d$, $d \in \{1, 2, 3\}$. η denotes events in the complete probabilistic space $(\hat{\Omega}, \hat{\mathcal{F}}, \hat{P})$, with $\hat{\mathcal{F}} \subset 2^{\hat{\Omega}}$ the σ -algebra of subsets of $\hat{\Omega}$ and \hat{P} a probability measure. $\Xi \subset \mathbb{R}^{N_\xi}$, is the stochastic space on which the random variables $\boldsymbol{\xi}(\eta)$ are defined and N_ξ stands for the number of random variables (two in our case under study).

The approach presented in this section is the Polynomial Chaos method. This method has been developed to solve Stochastic Differential and Partial Equations (SDE and SPDE, respectively).¹⁹ It was firstly introduced by Wiener,²⁰ in order to model through Hermite polynomials stochastic processes with gaussian random variables. Lately, Xiu & Karniadakis extended the original version of Wiener to a wider family of basis functions leading to the known concept of generalised Polynomial Chaos (gPC).⁷ It is also known as Askey-Chaos, due to the fact that is formed by the complete set of orthogonal polynomials from the Askey scheme.²¹ The objective of such extension is that for non-gaussian random inputs, the convergence of the Hermite-chaos is low, and in some cases, disastrous.

Polynomial Chaos is a spectral method and as such, an important advantage is that one may decompose a random representation into deterministic and stochastic components as

$$\hat{y}^{gPC}(\mathbf{x}, \boldsymbol{\xi}) = \sum_{j=0}^{\infty} y_{m_j}(\mathbf{x}) \Psi_j(\boldsymbol{\xi}), \quad (3)$$

where y_{m_j} are the deterministic coefficients (also called modal coefficients) with $\mathbf{x} = (x, r)$ and $\Psi_j(\boldsymbol{\xi})$ is the orthogonal base, in a tensor-like form by 1-D products of the orthogonal polynomials, satisfying the orthogonality relation

$$\langle \Psi_i, \Psi_j \rangle = \langle \Psi_i^2 \rangle \delta_{ij}, \quad (4)$$

with δ_{ij} the Kronecker delta function and $\langle \cdot, \cdot \rangle$ the inner product. In Eq. (3), the expansion has infinite terms. For practical reasons, this expansion has to be truncated accounting $N_t - 1$ terms, with

$$N_t = \frac{(N_\xi + P)!}{N_\xi! P!} \quad (5)$$

and P standing for the maximum order of the expansion. So that, the chaos expansion is finally expressed as

$$\hat{y}^{gPC}(\mathbf{x}, \boldsymbol{\xi}) = \sum_{j=0}^{N_t-1} y_{m_j}(\mathbf{x}) \Psi_j(\boldsymbol{\xi}). \quad (6)$$

In the following, we are going to get rid of \mathbf{x} and $\boldsymbol{\xi}$ just for sake of notation. Polynomial Chaos can be an Intrusive or Non-Intrusive approach. In this paper it is implemented as Non-Intrusive, due to the fact that it takes into account the solver as a black-box not requiring to code inside the CFD software. This has been a popular method in the recent years with many successful applications in literature.^{22,23,24} As the input uncertainties have been modelled by Uniform Probabilistic Distributions, Legendre polynomial basis functions are chosen. For the deterministic realisations required in the expansion, collocation points are chosen. Regarding the selection of the collocation point configuration, the use of Tensor Grids represents an expensive way. A much efficient mean is the use of sparse grids.²⁵ In this work, Clenshaw-Curtis (C-C) quadrature nested rule is applied²⁶ to generate the weights and nodes of the sparse grid. The coefficients y_{m_j} can now be computed as

$$y_{m_j} = \frac{\langle y, \Psi_j \rangle}{\langle \Psi_j^2 \rangle}. \quad (7)$$

The evaluation of Eq. (7) is in fact the computation of the multidimensional integral over the domain $\hat{\Omega}$, on which deterministic simulations of y from the CFD solver are required under prescription of the sparse grid. Moreover, this inner product is based on the measure of weights according to the choice of the orthogonal polynomials Ψ , as the weight function is in fact the probabilistic distribution function. As in the prescribed input uncertainties uniform distributions appear, the spectral method turns into a Polynomial Legendre Chaos. Once the coefficients are computed, the mean and the variance can be found by

$$\mathbb{E}(\hat{y}^{gPC}) = y_{m_0}, \quad (8)$$

$$\mathbb{V}(\hat{y}^{gPC}) = \sum_{j=1}^{N_t-1} y_{m_j}^2 \langle \Psi_j^2 \rangle. \quad (9)$$

An advantage of Polynomial chaos is that sensitivity analysis is straightforward from UQ results. This will be discussed in Section IV.

C. Kriging Surrogates for Uncertainty Quantification

Kriging (also known as Gaussian Process interpolation and in this paper under the acronym KG) is an interpolation surrogate method to approximate sets of data and it has been widely used in literature, specially for tasks involving costly computational analysis that by other methods would be expensive. Examples of this are CFD optimization,²⁷ sensitivity analysis,²⁸ topography²⁹ or prototyping.³⁰ Despite of the fact that surrogates can be also constructed with the Polynomial Chaos Expansion, the main idea of using Kriging is to try another method for a quick comparison. It is also possible hence to test whether Kriging surrogates can have a reliable behaviour with only a 65 deterministic simulations budget from collocation methods.

In essence, Kriging is a two-step process: first a regression function $f(\boldsymbol{\xi})$ is generated based on the data set, and from its residuals a Gaussian process $Z(\boldsymbol{\xi})$ is built, as can be seen in Eq. (10)

$$\hat{y}^{KG}(\boldsymbol{\xi}) = \hat{f}(\boldsymbol{\xi}) + Z(\boldsymbol{\xi}) = \sum_{i=1}^k \gamma_i f_i(\boldsymbol{\xi}) + Z(\boldsymbol{\xi}), \quad (10)$$

where $f(\boldsymbol{\xi})$ stands for the $k \times 1$ vector of basis regression functions $[f_1(\boldsymbol{\xi}) f_2(\boldsymbol{\xi}) \dots f_k(\boldsymbol{\xi})]$ and γ_i denotes the coefficients. Depending on the regression function, Kriging can be baptised with different names. Universal Kriging defines the trend function as a multivariate polynomial, as described in Eq. (10). Simple Kriging refers to the use of a known constant parameter as regression function, *i.e.* $f(\boldsymbol{\xi}) = 0$. A more popular version is Ordinary Kriging, which also assumes a constant but unknown regression function $f(\boldsymbol{\xi}) = \gamma_0$. Universal Kriging with a second order polynomial regression was our choice.

The Gaussian process $Z(\boldsymbol{\xi})$ is prescribed to have mean zero and $cov(Z(\xi_i), Z(\xi'_i)) = \sigma_p^2 R_c(\theta, \xi_i, \xi'_i)$, where σ_p^2 is the process variance and $R_c(\theta, \xi_i, \xi'_i)$ is the correlation model or spatial correlation function (SCF).

In order to create an accurate Kriging surrogate it is important to pay attention to the correlation function. This function only depends on the distance between the two points ξ_i and ξ'_i , and, for the general exponential case introduced in Eq. (11), also on p . The smaller the distance between two points, the higher the correlation and, hence, the more the Kriging predictor is influenced by the other. By the same token, if the distance gets bigger, the correlation drops to zero. For these reasons, it is not typically worthy to put several data points together, as the prediction would not be influenced. Several correlations can be tried, but in the present work the generalised exponential worked very well and was the final choice. From Eq. (11), exponential ($p = 1$) and gaussian ($p = 2$) are not appropriate for the complicated surrogates since during tests these gave some bumped areas in the spaces between nodes.

$$R_c(\theta, \xi_i, \xi'_i) = e^{-\theta|\xi_i - \xi'_i|^p} \quad (11)$$

For Kriging interpolation, the same Matlab code³¹ used by the first author in²⁷ has been utilised here with small modifications.

Because the shock-cells could create abrupt changes in some features, the generation of surrogates has been carefully tested. The best performance was observed for the general exponential correlation, whose results for complicated data sets to be interpolated can be seen in Fig. 10. It can be noticed that the surrogates have a smooth shape, so it is not expected to have substantial erratic contributions in uncertainty quantification when sampling inter nodal areas. In the following section, the application of sampling techniques and sensitivity analysis on Kriging surrogates is explained and a comparison between Kriging and SCM results is commented.

Once the Kriging surrogates are available, sampling techniques are affordable. Latin Hypercube Sampling³² and Random Sampling Monte Carlo are widely used non-intrusive methods for propagation of uncertainty in models (see Fig. 6). These methods have been used for many applications in science and a vast literature can be found. Generally speaking, sampling techniques evaluate the models \hat{y}^{KG} for different inputs $\boldsymbol{\xi}$, obtaining in that way the model predictions \hat{y}_i of a system

$$\hat{y}_i = \hat{y}^{KG}(\xi_i). \quad (12)$$

The goal of uncertainty analysis is to determine the uncertainty in \hat{y}^{KG} that results from uncertainty in the elements of $\boldsymbol{\xi}$. Those input uncertainties are represented by probabilistic distributions, on which the

sampling is done for the evaluations \hat{y}_i . From the evaluations of the model, a mapping of the performance is obtained, and a simple way of representing the output uncertainties can be to compute mean and variance as

$$\mathbb{E}(\hat{y}^{KG}) = \frac{1}{N_s} \sum_{i=1}^{N_s} \hat{y}_i, \quad (13)$$

$$\mathbb{V}(\hat{y}^{KG}) = \frac{1}{N_s - 1} \sum_{i=1}^{N_s} (\hat{y}_i - \mathbb{E}(\hat{y}^{KG}))^2. \quad (14)$$

It must be noticed that to compute $\mathbb{E}^{KG}(\hat{y})$ and $\mathbb{V}^{KG}(\hat{y})$ can be an incomplete representation of uncertainty in some cases, as two probabilistic distributions can have same mean and variance but very different shape. In our case under study we are not focusing on a particular point but the whole domain. For that reason it is better to represent the mean and variance contour plots.

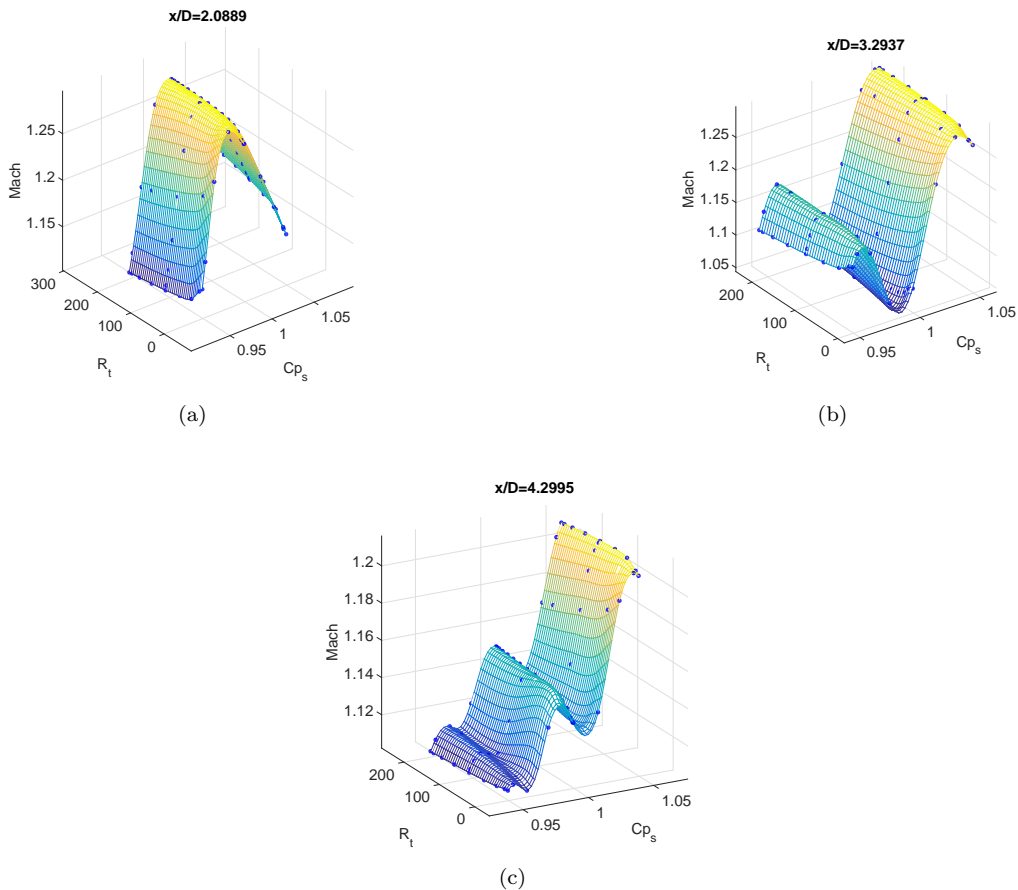


Figure 10. Examples of Kriging surrogates at several x/D distances on data sets with challenging shape. The blue points correspond to the deterministic CFD solutions from the fourth level of accuracy in the Clenshaw-Curtis sparse grid. In the plots Cp_s stands for the coefficient of variation for p_s ($\pm 5\%$).

D. Comparison and Discussion of Uncertainty Quantification Results

The first step for uncertainty quantification was to test the convergence of each method and do a comparison between the two methods. The idea behind using two different methods with different procedures (Kriging surrogate by sampling and gPC by quadrature on collocation points) is to provide a comparison. When focusing only on one method, any incoherent feature in the analysis or the codes could be taken as a conclusion that cannot be contrasted with any other result. However, if a second approach is giving similar outputs, a more consistent feedback can be extracted.

For this purpose, several samplings were tried on Kriging surrogates by Latin Hypercube Sampling (LHS) and the results were compared with the gPC expansion of 4th order (as $N_\xi = 2$, only 21 terms are required in the expansion). The accuracy of the methods has been tested along the lipline for the dimensionless axial velocity, v_x^* , and along the centreline for the Mach number, as these are the most relevant parts of the jet (along the centreline the shock-cells are strong and preliminary tests revealed that the nozzle lipline could be sensitive for v_x^*). To compute the integrals for the statistical moments of gPC, a sparse grid of 65 collocation points based on Clenshaw-Curtis (C-C) nested rule was used (the 65 collocation points correspond to the fourth level of accuracy), having a good match with Kriging sampled surrogates as shown in Figs. 11 and 12. The required number of collocation points was tested in,³³ computing the convergence of statistical moments with Stochastic Collocation Method, so that level of accuracy of the sparse grid was intended here for gPC.

For convergence of gPC, the order of the expansion, P , and the number of collocation points, N_q , have to be controlled. If N_q is fixed to the fourth level of accuracy (*lvl4*) as in the paragraph above, it is now necessary to focus on the order of the expansion, P , to compute the statistical moments. These undergo convergence up to $P = 4$. However, if $P > 4$, there is divergence and this is due to the fact that more collocation points are needed to compute the integrals. This has been tested numerically by means of generating artificial deterministic solutions from Kriging surrogates (see Fig. 13). With this procedure, the extra deterministic solutions of the sparse grid required for the fifth and sixth level of accuracy (*lvl5 artif* and *lvl6 artif* in the legend of the plots) are artificially generated and higher orders in the gPC expansion are tested. These plots are revealing that in fact in the region of $3 < x/D < 4$ more collocation points would be required with higher P . As for *lvl5* and *lvl6* are required 145 and 321 collocation points respectively with a not very relevant improvement in the accuracy, it is not worthy to perform such a large number of simulations with the CFD code and *lvl4* is assumed to be enough. Moreover, an adaptive refinement method³⁴ would not be worthy since the surrogates are different for each point of the domain.

Regarding the convergence of sampling on Kriging surrogates, even with a reduced number of samples, converged statistical moments can be obtained. This is because LHS is a sampling strategy more efficient than Monte-Carlo and also due to the fact that the stochastic dimension is low, requiring to sample less dimensions. Absolute errors are shown in the comparisons with gPC.

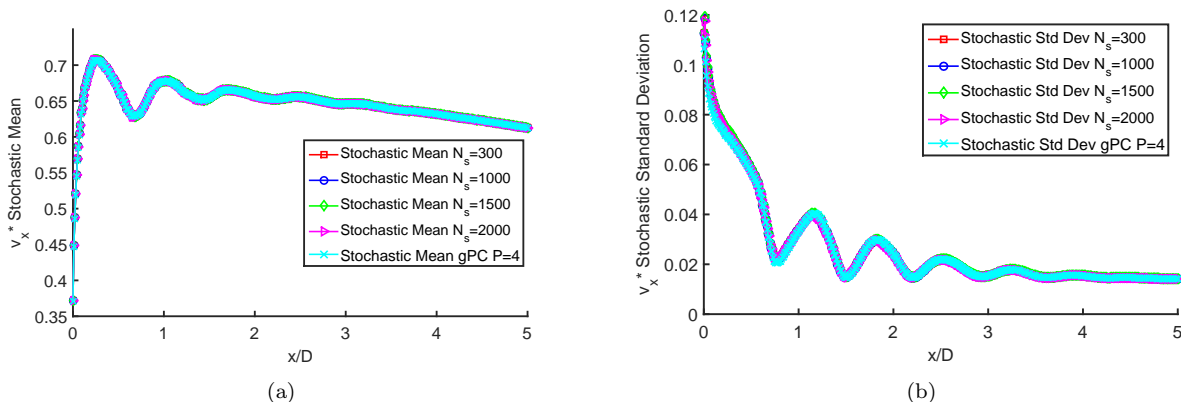


Figure 11. Evolution of the v_x^* stochastic means (a) and standard deviations (b) along the lipline for LHS on Kriging surrogates with different number of samples, N_s , and its comparison with gPC results. Even for a small number of samples, LHS is undergoing very good convergence.

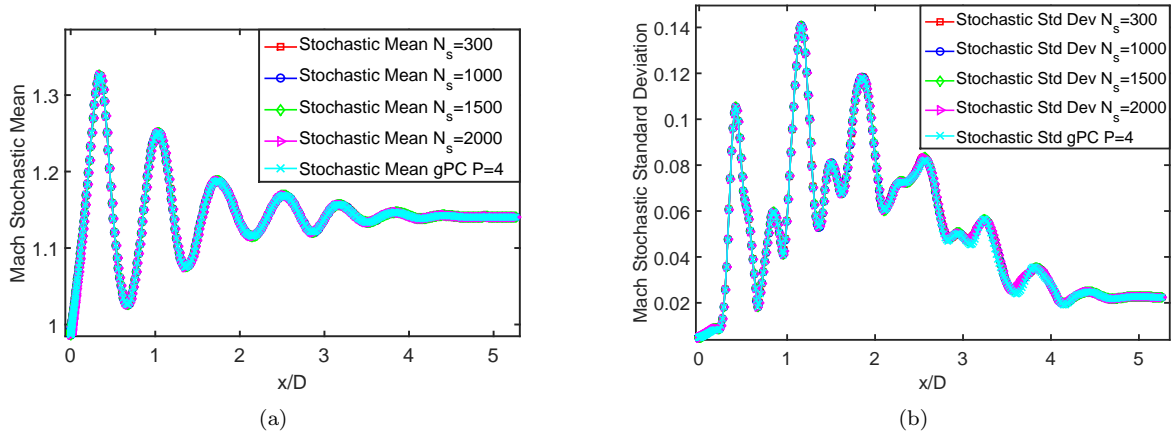


Figure 12. Evolution of the Mach stochastic means (a) and standard deviations (b) along the centreline for LHS on Kriging surrogates for different number of samples and its comparison with gPC results. Even for a small number of samples, LHS is undergoing very good convergence.

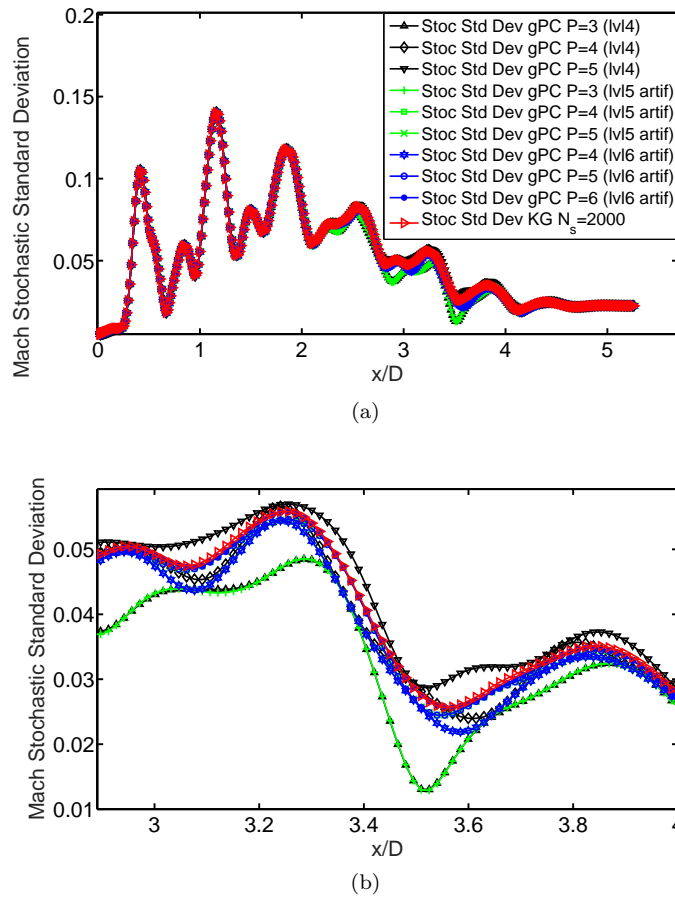


Figure 13. Evolution of (a) Mach stochastic standard deviation for different P and levels of the sparse grid and (b) a zoom of the most challenging part. These results are compared with Kriging surrogates sampled by means of LHS with $N_s = 2000$.

For the purpose of visualising uncertainty, the contour plots of the stochastic mean and variance are represented for both methods. In Figs. 14, 15 and 16 these values are plotted for v_x^* , v_r^* and p^* for Kriging surrogates only, as well as the absolute error with respect to gPC, which is showing the small difference in

the results between both methods.

Despite the absolute error in the variance can seem slightly notable, it is just illustrative. If attention is paid, i.e. on v_x^* along the lipline close to the nozzle in Fig. 14.d, the absolute error seems to be notable, but in Fig. 11 the difference is practically negligible.

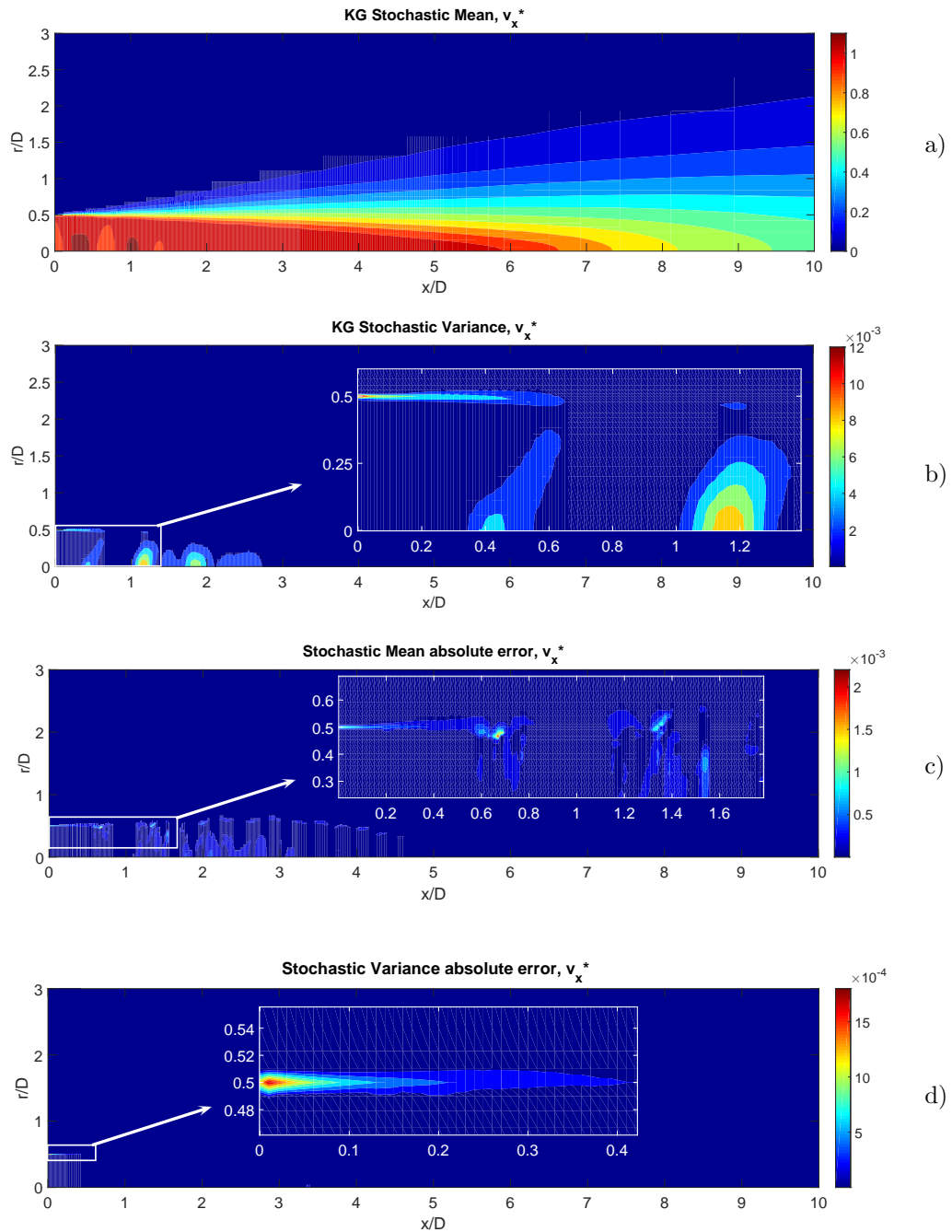


Figure 14. Contour plots of v_x^* (a) stochastic mean and (b) variance by means of LHS on KG surrogates. Contour plots of the absolute error between (c) stochastic mean and (d) variance between KG and gPC methods.

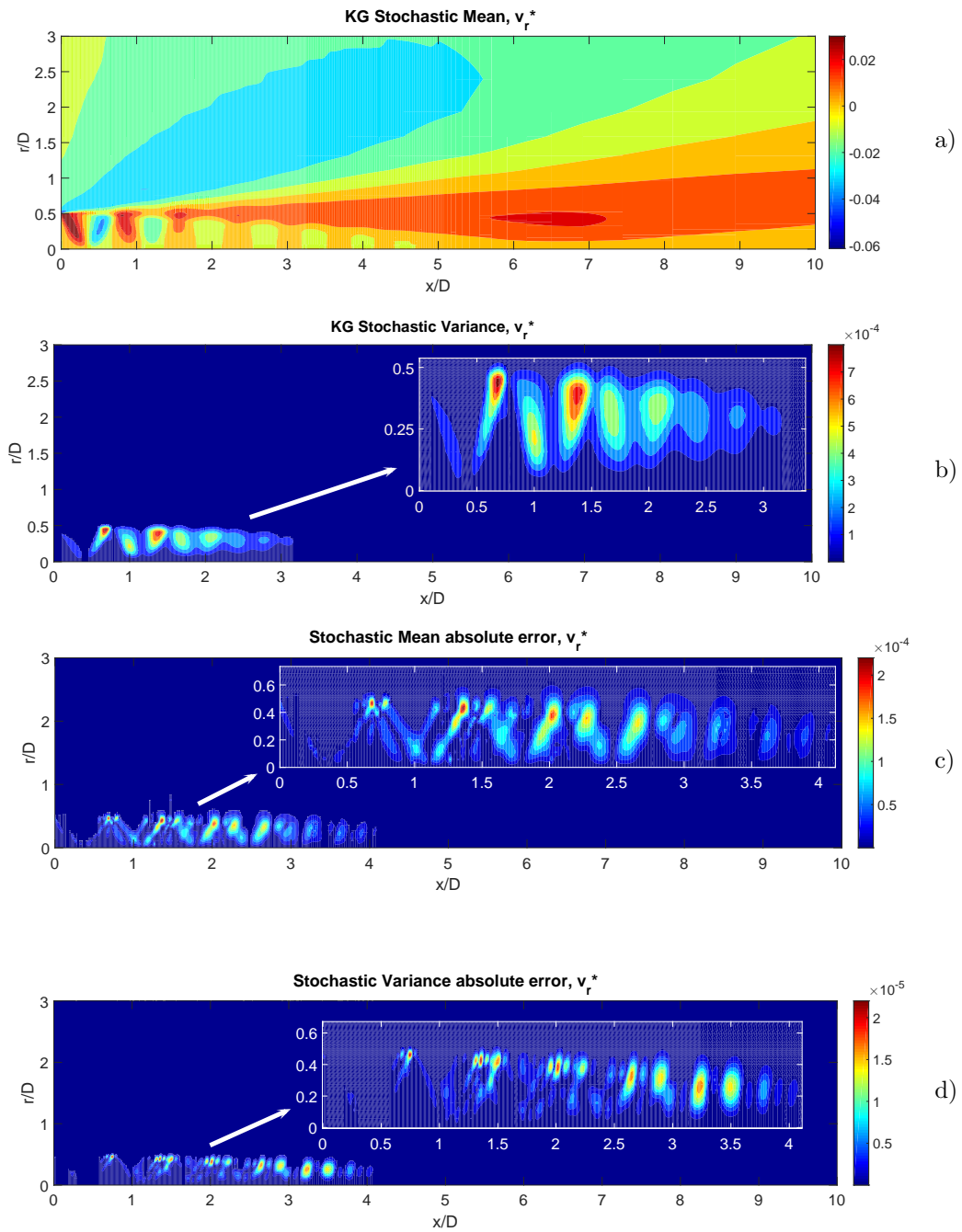


Figure 15. Contour plots of v_r^* (a) stochastic mean and (b) variance by means of LHS on KG surrogates. Contour plots of the absolute error between (c) stochastic mean and (d) variance between KG and gPC methods.

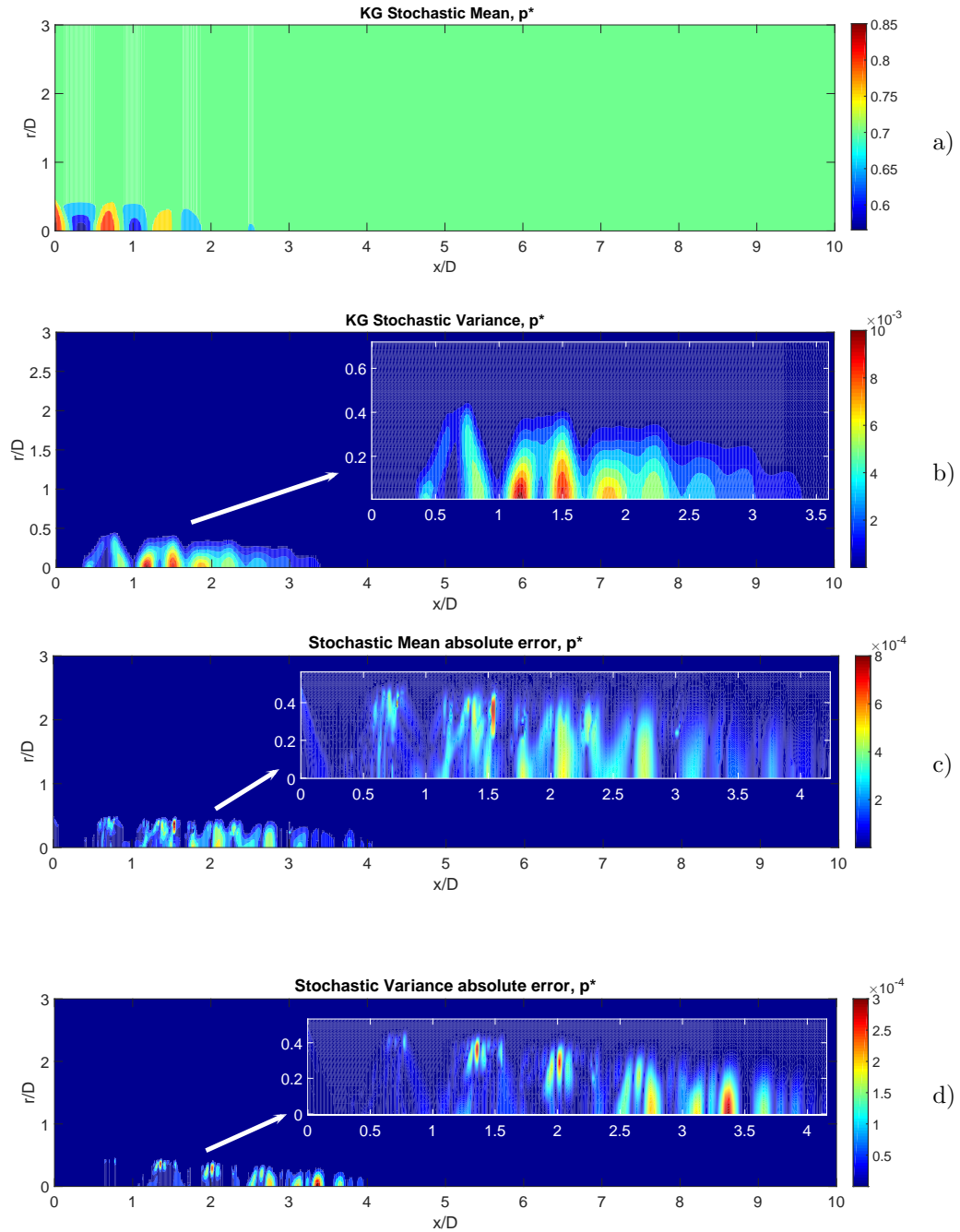


Figure 16. Contour plots of p^* (a) stochastic mean and (b) variance by means of LHS on KG surrogates. Contour plots of the absolute error between (c) stochastic mean and (d) variance between KG and gPC methods.

The objective of the analysis is to determine the regions of the jet which are more sensitive to the input uncertainties. From the task of understanding the physical meaning of the plots above, one can extract the following relevant information:

- For the dimensionless axial velocity, v_x^* , the most sensitive region is along the lipline, close to the nozzle lip (see Fig. 14.b). This uncertainty is in fact very high, as can be more clearly observed in Fig. 17.b. This finding can be influential for noise emission, especially for the screech noise feedback loop: when the vortical structures hit a shock-cell, there is a large pressure disturbance that can be propagated upstreams reaching the nozzle lip, and hence exciting the shear layer and generating new structures

that will propagate downstreams. For that reason, such uncertainty could be influential in near nozzle lip excitation and therefore affect the way screech noise is generated. In addition to this, since screech tone is a source of vibrations and resonance for nozzles, its uncertainty could be also influential in their lifespan. Along the centreline some uncertain regions can also be detected, but they can be better explained when describing the variance in p^* .

- Regarding the dimensionless radial velocity, v_r^* , the most sensitive region is immediately below the lipline (see Fig. 15.b). It is hard to associate this uncertainty to any particular phenomenon but it could influence the vortical structures. It can also be observed that the second and third shock-cell compression are notoriously the more sensitive to input uncertainty, where screech is usually generated.³⁵
- For the dimensionless static pressure, p^* , the most sensitive region is along the centreline (see Fig. 16.b). This is also observed for the Mach number in Fig. 17.a, where can also be noticed uncertainty in the position of the shocks. This situation can lead to the conclusion that shock-cell noise is affected somehow by the input uncertainties. Shock-cell noise is generated by the interaction between vortical structures and shock cells. This phenomenon can be affected by the uncertainty in the shock position, leading to the fact that peaks in the noise emission could be sort of flatten needing to share such energy in a broader frequency range. However, the axial and radial velocities (and hence the vortical structures) are also affected by the input uncertainties, what could also indicate the existence of higher values than expected in the noise peaks. This would therefore affect the robustness of the design.

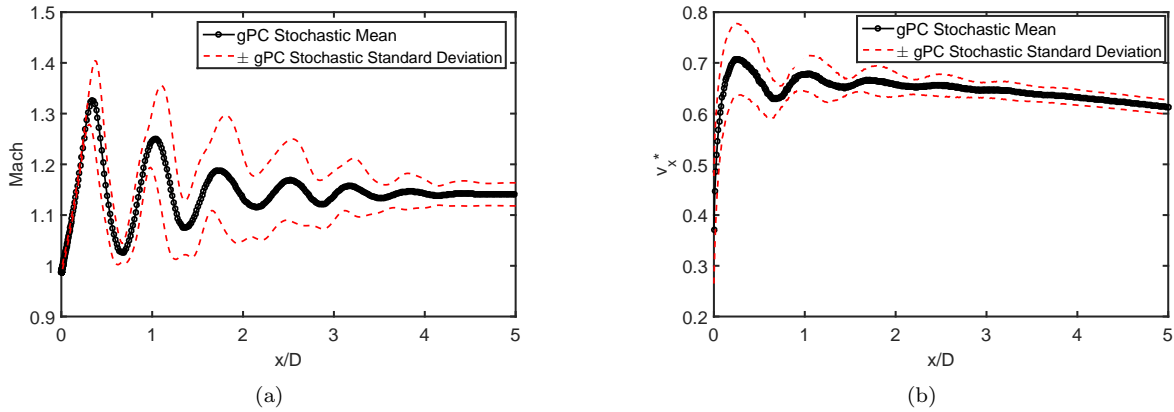


Figure 17. Stochastic mean and standard deviation envelopes with gPC for (a) Mach along centreline and (b) dimensionless axial velocity, v_x^* along the lipline.

IV. Sensitivity Analysis

An extension of UQ is the global Sensitivity Analysis (SA).³⁶ SA can be split into local or global methods. Local methods perform the sensitivity analysis by varying, commonly around a 5%, 10% or a value decided with the experience of the scientist, the values of a parameter in order to see how the output changes. On the other hand, the global analysis methods perform a sensitivity analysis not taking into account only the impact of the variation of one parameter, but also the higher-order effects in a wider range of the sampling. Despite of that, in literature is very common to see the use of local sensitivity analysis or OAT (One-factor-at-A-Time) methods.³⁷ This method has to be used very carefully, since when used, it is assumed that the model presents linearity, neglecting higher-order interactions. For further discussion between local and global methods, see.³⁸

There are different methods for global sensitivity analysis, such as Screening Method, Derivate Based Sensitivity Analysis or Variance-Based Analysis.³⁹ The scientist should choose the appropriate one depending on the computational cost, dimension of the problem or the expected output, among others. There is no general framework for this, which makes important for the scientist to understand all the possibilities and drawbacks.

For the purposes of this work, a Variance-Based Analysis has been chosen.⁴⁰ One of the main reasons of using this method is the possibility of ranking the influence of the input factors by sensitivity indices.

The ANOVA decomposition of the variance is shown in Eq. (15), and sensitivity coefficients are computed from Eq. (16) from its proportion with respect to the total variance. S_i and S_{T_i} , in Eq. (17), are the first-order and total sensitivity index respectively. In the following equations the multiple subscripts refer to second, third or higher order interactions, depending on the number of subscripts. Given a model of the form $y = \hat{y}(\xi_1, \xi_2, \dots, \xi_k)$, with y a scalar, the decomposition of the total variance, $\mathbb{V}(y)$, can be written as

$$\mathbb{V}(y) = \sum_{i=1}^{N_\xi} \mathbb{V}_{\xi_i} + \sum_{i=1, j>i}^{N_\xi} \mathbb{V}_{\xi_{ij}} + \sum_{i=1, k>j>i}^{N_\xi} \mathbb{V}_{\xi_{ijk}} + \dots \quad (15)$$

The values at the right hand side of the expression are the first and higher order contributions to the total variance. Dividing by the total variance, the sensitivities can be computed as

$$1 = \sum_{i=1}^{N_\xi} S_i + \sum_{i=1, j>i}^{N_\xi} S_{ij} + \sum_{i=1, k>j>i}^{N_\xi} S_{ijk} + \dots + S_{ijk, \dots, N_\xi}. \quad (16)$$

This leads to the following expression for the total sensitivity index for the i -th parameter

$$S_{T_i} = S_i + S_{ij} + S_{ijk} + \dots + S_{ijk\dots m} \quad (17)$$

and the associated sensitivity measure (first order sensitivity coefficient) is computed as

$$S_i = \frac{\mathbb{V}_{\xi_i}(\mathbb{E}_{\xi_{\sim i}}(y|\xi_i))}{\mathbb{V}(y)}, \quad (18)$$

where ξ_i is the i -th factor and $\xi_{\sim i}$ denotes the matrix of all factors but ξ_i . This index indicates by how much one could reduce on average the output variance if a parameter could be fixed. On the other hand, the total effect index can be computed as

$$S_{T_i} = \frac{\mathbb{E}_{\xi_{\sim i}}(\mathbb{V}_{\xi_i}(y|\xi_{\sim i}))}{\mathbb{V}(y)}. \quad (19)$$

S_{T_i} measures the total effect, *i.e.* first and higher order effects (interactions) of factor ξ_i . It represents a good measure to determine if a parameter is influential or not, and whether could be neglected from the model.

The use of this sensitivity technique can be seen in many fields such as solar energy,⁴¹ wastewater treatment,⁴² or heat exchangers.⁴³

As SA has relation with UQ, the approaches from Section III have been used in this section as well. Particularly, the Kriging surrogates are sampled according to⁴⁴ and the coefficients from gPC are used to compute the sensitivity indices. Despite that sampling could also be done on the Polynomial Chaos Expansion, it is worthy to remind that a second objective is to have two different methodologies to compare results (sampling and quadrature).

1. Generalised Polynomial Chaos for Sensitivity Analysis

One of the interesting features of gPC is the possibility of performing sensitivity analysis straightforward after uncertainty quantification. For such task, it is not difficult to realise that there is a clear relation between Eqs. (9), (15) and (16). Eq. (9) can be rewritten as

$$1 = \frac{1}{\mathbb{V}(\hat{y}^{gPC})} \sum_{j=1}^{N_t-1} y_{m_j}^2 \langle \Psi_j^2 \rangle, \quad (20)$$

and the first and higher-order sensitivity indices can carefully be extracted from the expression above since the literal part of each monomial gives the hints of the interaction.

2. Kriging surrogates for Sensitivity Analysis

Since the Kriging surrogates, \hat{y}^{KG} , are available from the uncertainty quantification study, it is now possible to compute the sensitivity indices from Eqs. (18) and (19).

In order to compute S_i , ξ_i has to be fixed in several points $\xi_i = \xi_i^*$ along the possible values of the random variable and compute the mean individually for a further computation of \mathbb{V}_{ξ_i} . This would require a very large number of calculations since the number of fixed points has to be great enough to compute reliable statistics. A less expensive method has been coded in Matlab by following the suggested procedure in.⁴⁴ With this method, the first order sensitivity with Kriging surrogates, S_i^{KG} , and the total effect, S_{Ti}^{KG} , can be computed as

$$S_i^{KG} = \frac{1 - \frac{1}{2N_s} \sum_{j=1}^{N_s} (\hat{y}^{KG}(B)_j - \hat{y}^{KG}(AB^i)_j)^2}{\mathbb{V}(\hat{y}^{KG})}, \quad (21)$$

$$S_{Ti}^{KG} = \frac{\frac{1}{2N_s} \sum_{j=1}^{N_s} (\hat{y}^{KG}(A)_j - \hat{y}^{KG}(AB^i)_j)^2}{\mathbb{V}(\hat{y}^{KG})}. \quad (22)$$

In these expressions, $\hat{y}^{KG}(A)$, $\hat{y}^{KG}(B)$ and $\hat{y}(AB)$ are model evaluated matrices, product of decomposition of the original matrices which contain the sample campaign. The procedure is as follows:

- Generate two independent Design of Experiment with LHS: A and B.
- The i-th column in matrix A is swapped with the i-th column in matrix B. AB^i is hence generated and the higher value of i is N_ξ .
- Evaluate the Kriging surrogates with the elements from the matrices A and B.
- In Eq. (21) and (22), j refers to the column of the matrices.

A. Comparison and Discussion of Sensitivity Analysis Results

As uncertainty quantification results were compared by means of Kriging surrogates and Polynomial Chaos in Section III, we decide to focus our attention now on the sensitivity contours with both methods for the dimensionless static pressure, p^* , plotted in Figs. 18 and 19.

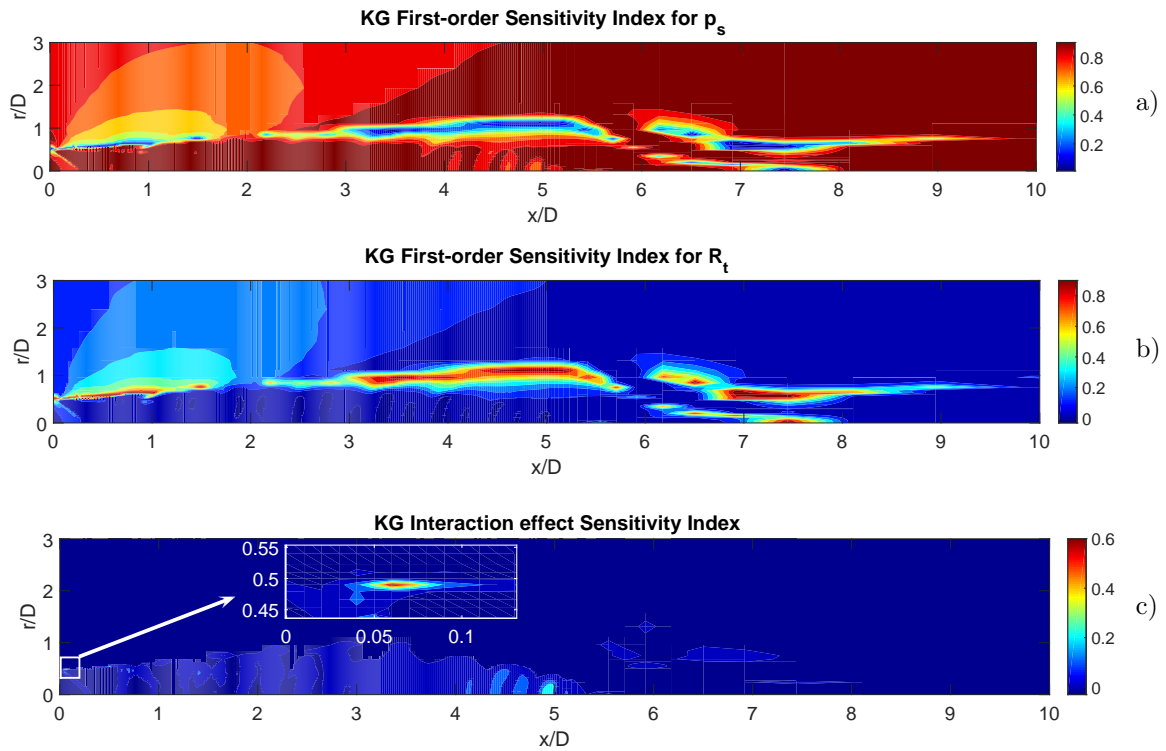


Figure 18. Sensitivity indices contour plots by means of Kriging for p^* . a) and b) are the first-order sensitivities and c) the higher-order interaction.

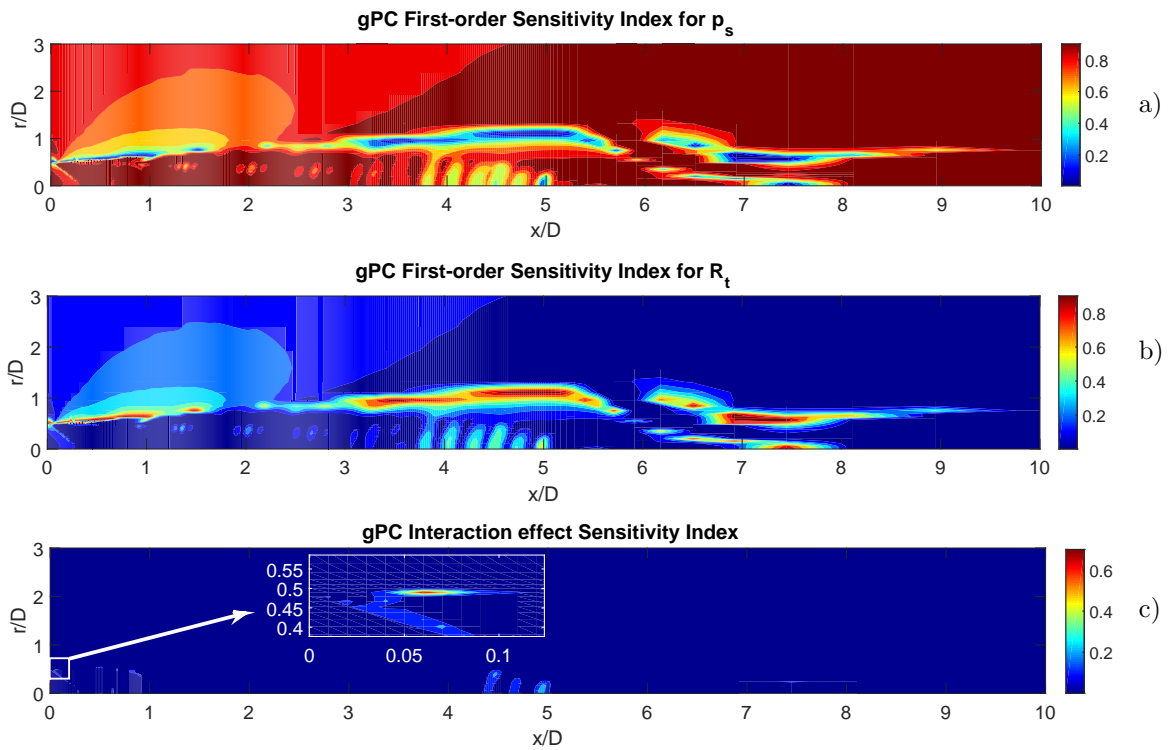


Figure 19. Sensitivity indices contour plots by means of gPC for p^* . a) and b) are the first-order sensitivities and c) the higher-order interaction.

One of the motivations of using two methods for sensitivity analysis purposes is that the resulting contours for the sensitivity indices were not intuitive, what could be product of errors implementing the codes. Fortunately, both methods provided similar solutions, discarding that. The explanation behind the contours appearance can be that, when performing sensitivity analysis, all the sensitivities of the domain are quantified simply providing a 'percentage' of contribution of uncertainty at every node of the CFD domain. A solution to provide a more intuitive and useful insight is to show the contribution to the total uncertainty by each parameter as shown in Figs. 20-22. For representation of the quantities of interest, this time only gPC results will be shown, as the errors between the implemented methods were checked in Section III and they were practically negligible.

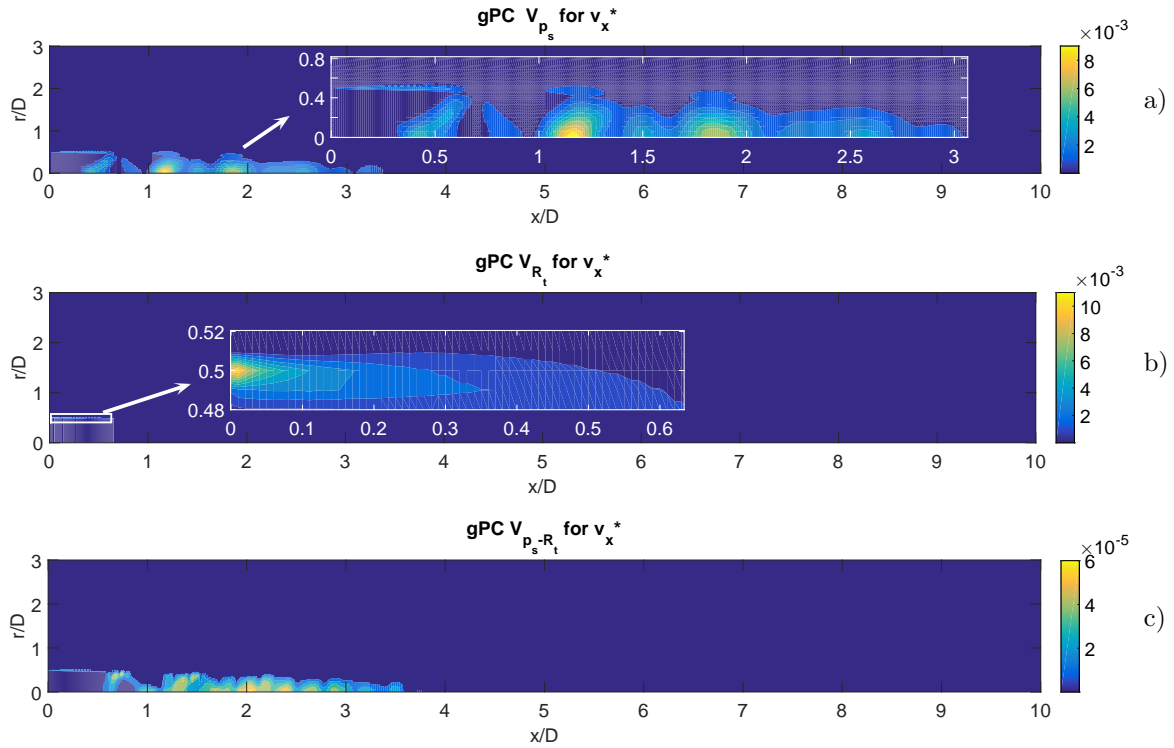


Figure 20. Contribution to the total variance of a) stagnation pressure, b) laminar to turbulent viscosity ratio and c) their interaction, for v_x^* .

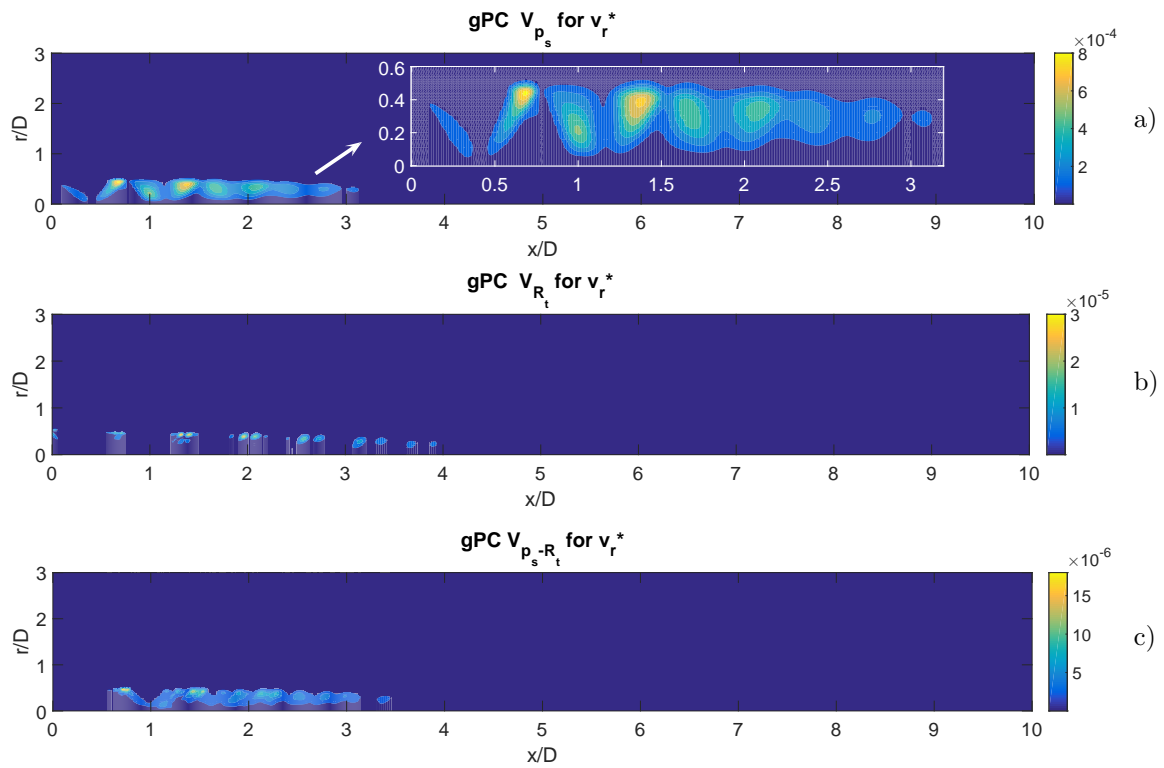


Figure 21. Contribution to the total variance of a) stagnation pressure, b) laminar to turbulent viscosity ratio and c) their interaction, for v_r^* .

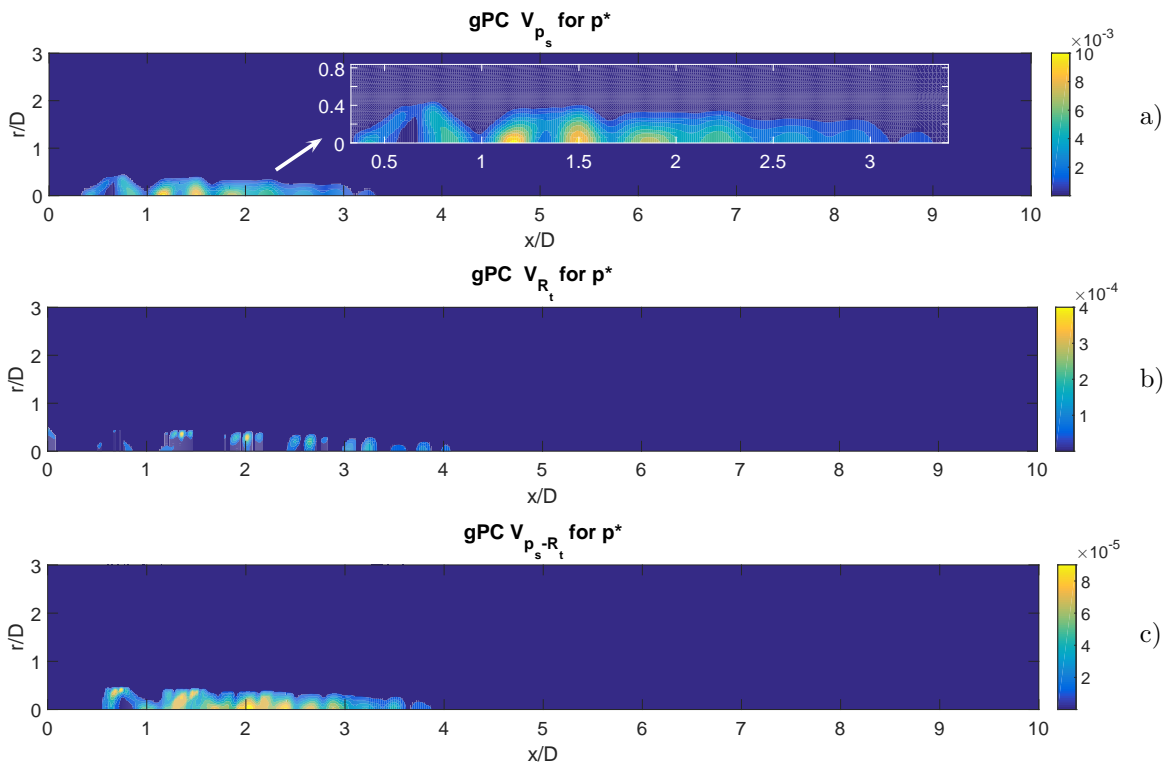


Figure 22. Contribution to the total variance of a) stagnation pressure, b) laminar to turbulent viscosity ratio and c) their interaction, for p^* .

In a similar manner than for uncertainty quantification, in this section several interesting patterns have been found linked to apportions to the input uncertainties:

- For the dimensionless axial velocity, v_x^* , the most sensitive region was detected along the lipline, close to the nozzle lip (see Fig. 14.b). This uncertainty is mainly due to uncertainty in the laminar to turbulent viscosity ratio, R_t , from the Spalart-Almaras turbulent model (see Fig. 20.b). The stagnation pressure uncertainty, p_s , is also playing an influential role (Fig. 20.a), but its impact is not as high as by R_t in the area immediately at the exhaust exit. The contribution to uncertainty in the shock-cell areas is done only by means of p_s uncertainty.
- Regarding the dimensionless radial velocity, v_r^* , the most sensitive region is immediately below the lipline (see Fig. 15.b). This uncertainty is undoubtedly linked to p_s as seen in Fig. 21.a.
- For the dimensionless static pressure, p^* , the most sensitive region is along the centreline (see Fig. 16.b). As can be seen in Fig. 22.a, p_s uncertainty is again the most influential one and the influence of R_t uncertainty is practically null. Closer to the lipline, R_t uncertainty is greater, but not very significant.

This analysis suggests that p_s uncertainty is a common factor in the three analysed uncertain flow parameters (dimensionless axial velocity, radial velocity and static pressure). This is especially notable in the shock-cell area and hence, possible hints about influence of p_s in shock-cell noise can be interpreted. Unfortunately, without higher-fidelity simulations such as LES or DNS, this cannot be confirmed, but this results leave such open question to be investigated.

V. Conclusions

Non-Intrusive Uncertainty Quantification techniques have been applied to 3D RANS CFD simulations of a supersonic under-expanded jet in order to understand the impact of input uncertainty (experimental and in turbulence modelling) affects to flow properties. Sensitivity Analysis was also carried out to understand the relevance of each random input in the output uncertainty. The results from the application of both methods (generalised Polynomial Chaos and Kriging with Latin Hypercube Sampling) have revealed a good match in the comparison. Despite the fact that shock-cells could be problematic for uncertainty quantification, convergence was achieved quickly and surrogates interpolate missing data in a very consistent way.

It has been relevant to extend this study to the whole CFD domain instead of relevant points, since some interesting regions such as the centre and lipline are sensitive and this study can lead to a deeper understanding of the flow physics in jets to motivate future investigations or paying more attention to developing more robust designs. In addition to this advantage in studying the whole domain, the stochastic base-flow here generated is to be taken under consideration for uncertainty quantification on Parabolised Stability Equations that model the jet flow instabilities.

From the points analysed in this paper, the following conclusions can be drawn:

- **Shock-cell position and amplitude is highly sensitive to input uncertainty.** This has been observed when the evolution of the Mach number was checked and the standard deviation envelopes were plotted. Moreover, this effect was also noticed in the contour plots of the variance for v_x^* , p^* and v_r^* , what could also be revealing a relation with uncertainty in the vortical structures. As shock-cell noise is generated by the interaction between vortical structures and shock-cells, the results presented here could be suggesting an important impact in such acoustic emission. With sensitivity analysis it has been observed that the uncertainty below the lipline (where the shock-cells are located) is mostly due to the uncertainty in the stagnation pressure.
- **The area immediately after the nozzle lip is highly sensitive to input uncertainty.** This outcome can be observed in the variance of v_x^* , where this interesting behaviour can be product of the pressure suction effect. The uncertainty in that region has to be taken into account, since this is

the location of the jet where the screech feedback loop takes place. These results reveal a stochastic behaviour that can be dramatically influential in the loop since it perturbs the shear-layer development. This could be also an influential fact in mixing noise. It has been also demonstrated that both the injection of turbulence and stagnation pressure imprecisions are actively contributing to that feature.

In addition to this, it can be observed in v_r^* high uncertainty immediately below the lipline, and the variance of stagnation pressure is the most influential parameter. This shows that the stochastic behaviour of the jet is 'stopping' the uncertainty spreading in the radial velocity at the lipline.

From this work, future research is encouraged. Since the turbulence effects are unsteady and local near the lip of the nozzle in high fidelity CFD simulations, such behaviour cannot be captured by RANS simulations and neither the acoustics. This has motivated a further study on UQ on jet stability by the authors, by using the results of this paper as stochastic base flow in order to understand the impact in the shear-layer perturbations, interesting for the screech feedback loop.

The stochastic behaviour of the vortical structures that generate noise interacting with shock-cells cannot be captured by RANS method. It is known that the interaction of the vortical structures and shock-cells drives acoustics and this should be analysed by LES or DNS simulations. But, at the moment, the computational resources to perform uncertainty quantification with such high-fidelity simulations of flows in the presence of shock-cells are very limited.

Acknowledgments

This research project is supported by a Marie Curie Initial Training Networks (ITN) AeroTraNet 2 of the European Community's Seventh Framework Programme (FP7) under contract number PITN-GA-2012-317142 that aims to generate a ready to use model for shock-cell noise characterization. The authors are thankful to Onera for licensing CERFACS to use the code *elsA* and to Daniel Guariglia (von Karman Institute for Fluid Dynamics) for the discussions about experimental uncertainty.

References

- ¹Gorle, C., Emory, M., and Iaccarino, G., "Epistemic uncertainty quantification of RANS modeling for an underexpanded jet in a supersonic cross flow," *CTR Annual Research Briefs, Center for Turbulence Research, Stanford University, Stanford, CA*, 2011.
- ²Witteveen, J. A., Doostan, A., Chantrasmı, T., Pecnik, R., and Iaccarino, G., "Comparison of stochastic collocation methods for uncertainty quantification of the transonic RAE 2822 airfoil," *Proceedings of workshop on quantification of CFD uncertainties*, 2009.
- ³Schaefer, J., West, T., Hosder, S., Rumsey, C., Carlson, J.-R., and Kleb, W., "Uncertainty Quantification of Turbulence Model Closure Coefficients for Transonic Wall-Bounded Flows," *22nd AIAA Computational Fluid Dynamics Conference*, 2015, p. 2461.
- ⁴Tam, C. K. and Burton, D. E., "Sound generated by instability waves of supersonic flows. Part 2. Axisymmetric jets," *Journal of Fluid Mechanics*, Vol. 138, 1984, pp. 273–295.
- ⁵Commission, E. et al., "Flightpath 2050. Europe's Vision for Aviation," Vol. –, 2012, pp. –.
- ⁶Cambier, L., Heib, S., and Plot, S., "The Onera elsA CFD software: input from research and feedback from industry," *Mech. & Ind.*, Vol. 14, No. 03, 2013, pp. 159–174.
- ⁷Xiu, D. and Karniadakis, G. E., "Modeling uncertainty in flow simulations via generalized polynomial chaos," *Journal of computational physics*, Vol. 187, No. 1, 2003, pp. 137–167.
- ⁸Spalart, P. and Allmaras, S., "A one-equation turbulence model for aerodynamic flows," *AIAA Paper 92-0439, 30th Aerospace Sciences Meeting and Exhibit, Reno, Nevada (1992)*, 1992.
- ⁹Roe, P. L., "Approximate Riemann solvers, parameter vectors and difference schemes," *Journal of Computational Physics*, Vol. 43, No. 2, 1981, pp. 357–372.
- ¹⁰van Leer, B., "Towards the ultimate conservative difference scheme. V. A second-order sequel to Godunov's method," *Journal of Computational Physics*, Vol. 32, No. 1, 1979, pp. 101–136.
- ¹¹Chakravarthy, S., "High resolution upwind formulations for the Navier-Stokes equations," *Computational Fluid Dynamics, VKI Lecture Series 1988-05, March 711*, 1988.
- ¹²Harten, A., "High resolution scheme for hyperbolic conservation laws," *Journal of Computational Physics*, Vol. 49, 1983, pp. 357–393.
- ¹³Larrouturou, B., "How to preserve the mass fractions positivity when computing compressible multi-component flows," *Journal of Computational Physics*, Vol. 95, 1991, pp. 59–84.

- ¹⁴Weber, C., *Développement de méthodes implicites pour les équations de Navier-Stokes moyennes et la simulation des grandes échelles : Application à l'aérodynamique externe*, Ph.D. thesis, Institut National Polytechnique de Toulouse, France, 1998.
- ¹⁵André, B., Castelain, T., and Bailly, C., "Broadband Shock-Associated Noise in Screeching and Non-Screeching Under-expanded Supersonic Jets," *AIAA J.*, Vol. 51, No. 3, 2013, pp. 665–673.
- ¹⁶Saltelli, A., Tarantola, S., Campolongo, F., and Ratto, M., *Sensitivity Analysis in Practice: A Guide to Assessing Scientific Models*, John Wiley & Sons, Ltd., 2004.
- ¹⁷Pérez Arroyo, C., Daviller, G., Puigt, G., and Airiau, C., "Shock-cell noise of supersonic under expanded jets," *50th 3AF International Conference on Applied Aerodynamics*, Toulouse, France, 29-30 March - 1 April 2015, conf.
- ¹⁸Pérez Arroyo, C., Daviller, G., Puigt, G., and Airiau, C., "Modal structure of a supersonic under-expanded jet," *22ème Congrès Français de Mécanique, 24 - 28 August, Lyon, France*, 2015.
- ¹⁹Spanos, P. D. and Ghanem, R., "Stochastic finite element expansion for random media," *Journal of engineering mechanics*, Vol. 115, No. 5, 1989, pp. 1035–1053.
- ²⁰Wiener, N., "The homogeneous chaos," *American Journal of Mathematics*, Vol. 60, No. 4, 1938, pp. 897–936.
- ²¹Askey, R. and Wilson, J., "Some Basic Hypergeometric Polynomials That Generalize Jacobi Polynomials, Vol. 319," *Mem. Amer. Math., Providence, RI*, 1985.
- ²²Congedo, P. M., Duprat, C., Balarac, G., and Corre, C., "Effects of inlet uncertainties on prediction of turbulent flows using RANS and LES simulations," *20th AIAA Computational Fluid Dynamics Conference*, 2011, p. 3869.
- ²³Lucor, D., Meyers, J., and Sagaut, P., "Sensitivity analysis of large-eddy simulations to subgrid-scale-model parametric uncertainty using polynomial chaos," *Journal of Fluid Mechanics*, Vol. 585, 2007, pp. 255–279.
- ²⁴Eldred, M. and Burkardt, J., "Comparison of non-intrusive polynomial chaos and stochastic collocation methods for uncertainty quantification," *AIAA paper*, Vol. 976, No. 2009, 2009, pp. 1–20.
- ²⁵Smolyak, S., "Quadrature and interpolation formulas for tensor products of certain classes of functions," *Soviet Math. Dokl.*, 1963, pp. 240–243.
- ²⁶Von Winckel, G., "Fast Clenshaw-Curtis quadrature," Tech. rep., The Mathworks Central File Exchange, Mar. 2008. URL <http://www.mathworks.com/matlabcentral/fileexchange/19063-sparse-grid-quadrature/content/spquad.m>, 2008.
- ²⁷Granados-Ortiz, F.-J., Ortega-Casanova, J., and Lai, C.-H., "Modelling for Computational Cost Reduction and Optimisation of an Impinging Swirling Jet created by a Rotating Pipe with Application to Heat Transfer from a Heated Solid Flat Plate," *8th International Congress on Industrial and Applied Mathematics. Beijing, (China). 10-14 August 2015*, 2015.
- ²⁸Warnes, J. J., "A sensitivity analysis for universal kriging," *Mathematical Geology*, Vol. 18, No. 7, 1986, pp. 653–676.
- ²⁹Legleiter, C. J. and Kyriakidis, P. C., "Spatial prediction of river channel topography by kriging," *Earth Surface Processes and Landforms*, Vol. 33, No. 6, 2008, pp. 841–867.
- ³⁰Hiemstra, P. H., Pebesma, E. J., Twenhöfel, C. J., and Heuvelink, G. B., "Automatic real-time interpolation of radiation hazards: prototype and system architecture considerations," *International Journal of Spatial Data Infrastructures Research*, Vol. 3, 2008, pp. 58–72.
- ³¹Lophaven, S. N., Nielsen, H. B., and Sndergaard, J., "DACE: A MATLAB Kriging Toolbox. Version 2.0," Tech. rep., DTU, 2002, Tech. Report NASA/CR-2003-212153, NASA Langley Research Center.
- ³²Helton, J. and Davis, F., "Latin hypercube sampling and the propagation of uncertainty in analyses of complex systems," *Reliability Engineering and System Safety*, Vol. 81, 2003, pp. 23–69.
- ³³Granados-Ortiz, F.-J. and Lai, C.-H., "A Novel Framework for Uncertainty Propagation in Multidisciplinary Design Life Cycle for Shock-Cell Noise Research," *22nd CEAS/AIAA Aeroacoustics 2016, Lyon, France*, 2016.
- ³⁴Witteveen, J. A. and Iaccarino, G., "Simplex stochastic collocation with ENO-type stencil selection for robust uncertainty quantification," *Journal of Computational Physics*, Vol. 239, 2013, pp. 1–21.
- ³⁵Panda, J., "Shock oscillation in underexpanded screeching jets," *J. Fluid Mech.*, Vol. 363, 1998, pp. 173–198.
- ³⁶Saltelli, A., Ratto, M., Andres, T., Campolongo, F., Cariboni, J., Gatelli, D., and Tarantola, S., *Global sensitivity analysis: the primer*, John Wiley & Sons, 2008.
- ³⁷Mouida, A. and Alaa, N., "Sensitivity Analysis of TSEB Model by One-Factor-At-A-Time in irrigated olive orchard," *International Journal of Computer Science Issues*, 2011.
- ³⁸Kent, E., Neumann, S., Kummer, U., and Mendes, P., "What Can We Learn from Global Sensitivity Analysis of Biochemical Systems?" *PLoS ONE* 8(11): e79244. doi:10.1371/journal.pone.0079244, 2013.
- ³⁹Tian, W., "A review of sensitivity analysis methods in building energy analysis," *Renewable Sustainable Energy Rev*, Vol. 20, 2013, pp. 4–119.
- ⁴⁰Saltelli, A., "Variance based sensitivity analysis of model output. Design and estimator for the total sensitivity index," *Computer Physics Communications*, 2009.
- ⁴¹Silva, R., Perez, M., Berenguel, M., Valenzuela, L., and Zarza, E., "Uncertainty and global sensitivity analysis in the design of parabolic-through direct steam generation plants for process heat applications," *Applied Energy*, Vol. 121, 2014, pp. 233–244.
- ⁴²Sin, G., Gernaey, K. V., Neumann, M. B., van Loosdrecht, M. C. M., and Gujer, W., "Global sensitivity analysis in waste water treatment plant model applications: Prioritizing sources of uncertainty," *Water Research*, Vol. 45, No. 2, 2011, pp. 639–651.
- ⁴³Fesanghary, M., Damangir, E., and Soleimani, I., "Design optimization of shell and tube heat exchangers using global sensitivity analysis and harmony search algorithm," *Applied Thermal Engineering*, Vol. 29, No. 5, 2009, pp. 1026–1031.
- ⁴⁴Jansen, M. J., "Analysis of variance designs for model output," *Computer Physics Communications*, Vol. 117, No. 1, 1999, pp. 35–43.